JGR Planets

RESEARCH ARTICLE
10.1029/2021JE007023

Special Section:
The Curiosity rover's investigation of Glen Torridon and the surrounding area

Evidence for Fluctuating Wind in Shaping an Ancient Martian Dune Field: The Stimson Formation at the Greenheugh Pediment, Gale Crater

Steven G. Banham[1], Sanjeev Gupta[1], David M. Rubin[2], Candice C. Bedford[3,4], Lauren A. Edgar[5], Alex B. Bryk[6], William E. Dietrich[6], Christopher M. Fedo[7], Rebecca M. Williams[8], Gwénaël Caravaca[9], Robert Barnes[1], Gerhard Paar[10], Thomas Ortner[11], and Ashwin R. Vasavada[12]

[1]Department of Earth Sciences and Engineering, Imperial College London, London, UK, [2]Department of Earth and Planetary Sciences, University of California, Santa Cruz, CA, USA, [3]NASA Johnson Space Center, Houston, TX, USA, [4]Lunar and Planetary Institute, Universities Space Research Association, Houston, TX, USA, [5]U.S. Geological Survey, Astrogeology Science Center, Flagstaff, AZ, USA, [6]Earth & Planetary Science, University of California Berkeley, Berkeley, CA, USA, [7]Department of Earth and Planetary Sciences, University of Tennessee Knoxville, Knoxville, TN, USA, [8]Planetary Science Institute, Tucson, AZ, USA, [9]UMR 5277 CNRS, UPS, CNES Institut de Recherche en Astrophysique et Planétologie, Université Paul Sabatier Toulouse III, Toulouse, France, [10]JOANNEUM RESEARCH Institute for Information- and Communication Technologies, Graz, Austria, [11]VRVis zentrum für virtual reality und visualisierung forschungs gmbh, Vienna, Austria, [12]Jet Propulsion Laboratory, California Institute of Technology, Pasadena, CA, USA

Abstract Temporal fluctuations of wind strength and direction can influence aeolian bedform morphology and orientation, which can be encoded into the architecture of aeolian deposits. These strata represent a direct record of atmospheric processes and can be used to understand ancient Martian atmospheric processes as well as those on Earth. The strata can: give insight to ancient atmospheric circulation, how the atmosphere evolved in response to global changes in habitability, and how ancient processes differ from modern processes. The Stimson formation at the Greenheugh pediment (Gale crater) records evidence of fluctuating wind across multiple temporal scales. The strata can be subdivided into three intervals–Gleann Beag, Ladder, and Edinburgh intervals. Internally, the intervals record changes of dune morphology and orientation, correlatable to wind fluctuations at multiple temporal scales. The basal Gleann Beag interval comprises compound cross-strata, deposited by oblique compound dunes. These dunes record a bimodal wind regime, resulting in net sediment transport toward the north. The Ladder interval records a reversal of sediment transport to the south, where straight-crested simple-dunes shaped by a seasonally variable winds formed. Finally, the Edinburgh interval records sediment transport to the west, where a unimodal wind formed sinuous-crested simple dunes. These observations demonstrate active and variable atmospheric circulation in Gale crater during the accumulation of the Stimson dune field, at multiple temporal scales from seasonally driven winds to much longer time-frames, during the Hesperian. These observations can be used to further understand ancient atmospheric conditions and processes, at a high temporal resolution on Mars.

Plain Language Summary The direction and strength of the wind varies, but typically follows predictable patterns over a variety of time-scales ranging from the course of a day or a year through to decades or millennia. Within a dune field, these patterns of air flow control the shape, size and orientation of aeolian landforms-such as dunes and ripples–and in-turn be recorded in the rock record, where sediment accumulates over time. These deposits form a record of ancient atmospheric processes, and can be found on Mars, as well as Earth. On Mars, within the Stimson sandstone, evidence for short- and long-term wind trends are identified in these strata deposited by ancient dunes. This partial record–resulting from episodic erosion and deposition characteristic of dune migration–indicates dunes were shaped by seasonal and longer-term sediment transport processes, and that the shape of dunes, and their orientation changed in response long-term changes in wind direction. These changing winds give us insight to the prevailing climate controlling the wind within Gale crater during the Hesperian period and can be used to constrain climate models and gain insight to habitability at that time.

Key Points:

- The Greenheugh pediment capping unit is part of the Stimson formation, containing architectural elements consistent with aeolian processes
- Here, the formation is subdivided into three intervals based on sedimentary architecture: Gleann Beag, Ladder and Edinburgh intervals
- The preserved architecture is a product of fluctuating wind at multiple temporal scales, recording seasonal through to millennial cycles

Supporting Information:

Supporting Information may be found in the online version of this article.

Correspondence to:

S. G. Banham,
s.banham@imperial.ac.uk

Citation:

Banham, S. G., Gupta, S., Rubin, D. M., Bedford, C. C., Edgar, L. A., Bryk, A. B., et al. (2022). Evidence for fluctuating wind in shaping an ancient Martian dune field: The Stimson formation at the Greenheugh pediment, Gale crater. *Journal of Geophysical Research: Planets*, *127*, e2021JE007023. https://doi.org/10.1029/2021JE007023

Received 18 OCT 2021
Accepted 17 JUN 2022

Author Contributions:

Conceptualization: Steven G. Banham
Funding acquisition: Steven G. Banham, Ashwin R. Vasavada
Investigation: Steven G. Banham, Ashwin R. Vasavada
Methodology: Steven G. Banham, Ashwin R. Vasavada

Project Administration: Ashwin R. Vasavada
Software: Robert Barnes, Gerhard Paar, Thomas Ortner
Visualization: Robert Barnes, Gerhard Paar
Writing – original draft: Steven G. Banham
Writing – review & editing: Steven G. Banham, Gerhard Paar, Ashwin R. Vasavada

1. Introduction

Aeolian dune fields are shaped by the whims and rhythms of the wind, which rarely blows uniformly or exclusively from a single direction. It is common for the wind direction and strength to vary, dictated by a multitude of factors operating at a range of timescales. These time-scales can range from diurnal fluctuations, recorded by wind ripple migration (Hunter & Richmond, 1988) to more prolonged seasonal (annual) wind variations (Hunter & Rubin, 1983), which can result in episodes of oblique or reversed airflow and create discontinuities on a dune's lee face (Kocurek, 1991). Longer-term trends driven by changes in the local, regional, or global climate can result in prolonged changes to the wind regime, and the long-term sediment transport direction, which can cause partial or complete realignment of dunes within a dune field, causing dunes to migrate in completely different directions to their predecessors. These changes in the wind, from wind-ripples responding to daily cycles, to compound dunes (also referred to as mega dunes, or as draas) responding to decadal or centennial changes in wind direction can be recorded in the stratigraphy. Frequent, short-duration changes may be recorded by variations of facies interstratification. Longer-duration, less-frequent fluctuations may cause a change in cross-set morphology (compound vs. simple) or reorientation of cross-bedding dip-azimuths.

As well as controlling dune orientation, changes of wind direction can lead to changes in the sediment transport direction and availability, which can result in profound changes to the pattern of sediment accumulation. Changes of wind direction can starve sediment supply to the dune field, leading to episodes of dune bypass or deflation, whereupon accumulated sediment is removed from the depositional record, forming deflational supersurfaces. These signatures of variable wind direction have been identified within the terrestrial stratigraphic record (Chan et al., 2000; Kocurek, 1991; Mountney & Thompson, 2002; Scherer & Goldberg, 2010) and can provide insight to past atmospheric circulation and processes, but thus far there are few documented examples of fluctuating or reversal of wind directions preserved in the Martian stratigraphic record (Banham et al., 2021; Hayes et al., 2011). Recognizing such features in the Martian stratigraphic record could be used to reconstruct ancient atmospheric processes that occurred during Mars' early history, when habitability was more likely.

Banham et al. (2018) documented the presence a major aeolian dune field which existed in Gale crater, represented by the preserved stratigraphic remnants of the Stimson formation. The Stimson formation contains depositional packages and erosional surfaces directly linkable to surface processes, and landforms, such as dune morphology and orientation, which reflect the ancient wind regime. Using the Mars Science Laboratory (MSL) Curiosity rover, the Stimson formation on the northern edge of the Greenheugh pediment (Figure 1a), was documented between Sols 2618 and 2780. These data are used to investigate the origin of the sandstone capping unit, and the processes that are recorded by its internal stratigraphic architecture.

The specific objectives of this study are to: (a) determine the sediment transport processes from textural observations; (b) reconstruct dune morphology, size, and orientation, based on the sedimentary architecture; (c) understand the temporal evolution of the dune field, and how variations of wind direction are recorded; (d) comment on the stratigraphic relationship of the Stimson formation at the Greenheugh pediment, and other Stimson outcrops observed by Curiosity during the traverse.

2. Background and Geological Setting

Gale crater is located on the Martian crustal dichotomy boundary, at 5.4°S, 137.8°E. Gale is ∼154 km in diameter and was formed 3.7 Ga (+/− 0.1 Ga), which coincides with the Noachian-Hesperian transition period (Le Deit et al., 2013; Tanaka et al., 2014; Thomson et al., 2011). Sediment accumulated in Gale in the 200–500 Myr following crater formation (Grant et al., 2014; Grotzinger, Gupta, et al., 2015; Thomson et al., 2011). The preserved remnants of the infilling of the crater is represented as the ∼5 km height, stratified, sediment pile which forms Aeolis Mons (informally Mount Sharp) (Anderson & Bell, 2010). The lower strata, including those on Aeolis Palus, include fluvial, deltaic and lacustrine sediments (Grotzinger, Crisp, et al., 2015). The upper strata of Aeolis Mons include sulfate-bearing rocks which contains meter-scale cross-bedded sedimentary rocks (Milliken et al., 2014; Rapin et al., 2021), and yardang-forming strata with cross-bedded strata (Anderson et al., 2018; Dromart et al., 2018; Rapin et al., 2021). Key observations relating to the sediment pile

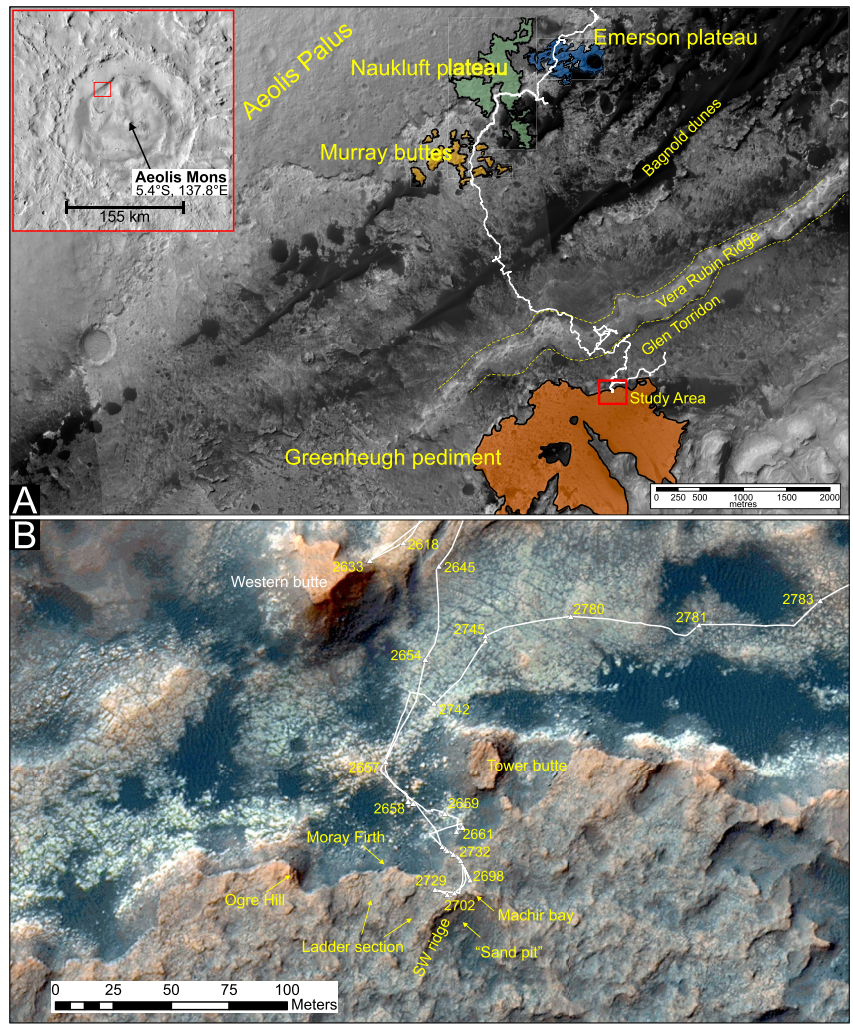

Figure 1. Overview orthomosaics of the study area. (a) High-resolution Imaging Science Experiment (HiRISE) satellite mosaic showing the region of the traverse within Gale crater, showing the spatial relationship between the northern Stimson formation outcrops (Emerson plateau, Naukluft plateau, and Murray buttes), and the Greenheugh pediment higher on the north flank of Aeolis Mons. Inset map is a CTX mosaic showing the location of the traverse within the context of Gale crater. (b) Detailed HiRISE orthomosaic of the study area, showing locations of the rover between sols 2618 and 2783. The map highlights key outcrop locations discussed in this paper. Base maps, MSL Gale Merged Orthophoto Mosaic 25 m was generated by Calef and Parker (2016). Image credit: NASA/JPL/University of Arizona.

forming Aeolis Mons are: the sediments are lithified up to the summit; these sediments are fractured, implying diagenetic fluid movement; and that cross-bedded sediments accumulated on the flanks of the degraded sediment pile.

As of January 2021, the stratigraphy of lower Aeolis Mons–based on the MSL science team's interpretation–(Figure 1a) is subdivided into the following lithostratigraphic groups: Bradbury, Mount Sharp, and Siccar Point. As the beds are mostly flat-lying, vertical elevation has been used as a proxy for stratigraphic position. The Bradbury group (the lowest observed 70 m of the succession) is interpreted to be interfingering deltaic, fluvial, and lacustrine sedimentary rocks (Edgar et al., 2017; Grotzinger et al., 2014; Grotzinger, Gupta, et al., 2015; Schieber et al., 2017) (Figure 2). The Mount Sharp group is the next stratigraphic unit that the rover traversed after the Bradbury group. The lowest unit in this group is the Murray formation, which represents the lowermost >300 m of the succession. It is composed of laminated lacustrine mudstones, with minor intraformational fluvial sediments (Edgar et al., 2020; Grotzinger, Gupta, et al., 2015; Stack et al., 2019). Conformably overlying the Murray formation is the Carolyn Shoemaker formation (also referred herein as the C.Shoemaker formation), which

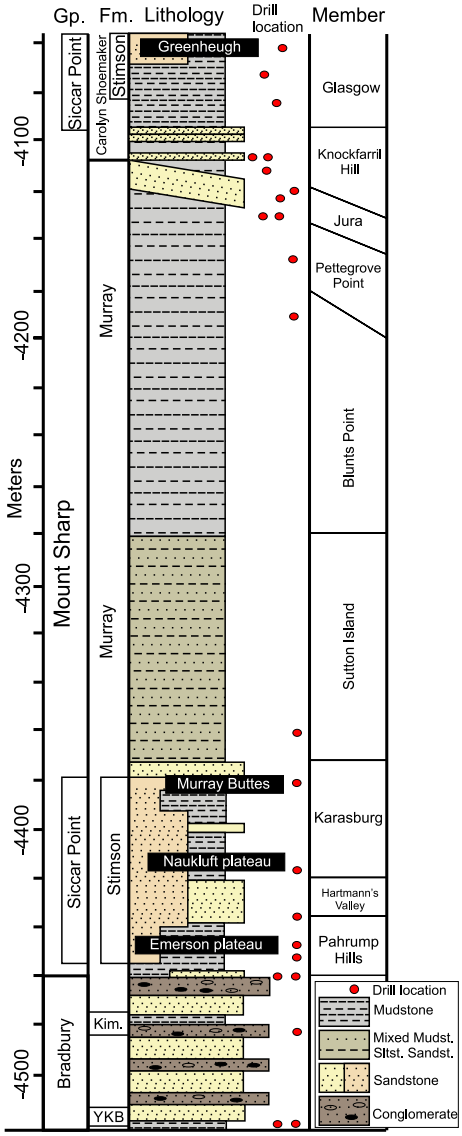

Figure 2. Stratigraphic context of the Stimson formation within the stratigraphic framework erected by the MSL team. The stratigraphic column depicts key stratigraphic units encountered by the rover during the mission. The column shows units associated with the vertical elevation and does not account for total stratigraphic thickness. Members referred to form components of the Murray and Carolyn Shoemaker formations. For more details see Fedo et al., 2022; Caravaca et al., 2022; Bennett et al., 2022.

is composed of horizontally laminated siltstones and sandstones, and an increased proportion of fluvial and aeolian sandstones (Bennett et al., 2022). The Murray formation is subdivided into seven members, which are interpreted to record lake and lake margin environments. These are: Pahrump Hills (Stack et al., 2019); Hartmann's Valley (Gwizd et al., 2018, 2022); Karasburg (Gwizd et al., 2020, 2022) Sutton island (Edgar et al., 2020; Fedo et al., 2017), and Pettegrove Point members. Blunts Point and the Jura members of the Murray formation comprise the landform known as the Vera Rubin Ridge (Edgar et al., 2020; Fedo et al., 2020; Fraeman et al., 2020), which underwent some degree of diagenesis to form a prominent topographic feature (Fraeman et al., 2016, 2020). The base of the Carolyn Shoemaker formation is coincident with the base of the Knockfarril Hill member, in the topographic low known as Glen Torridon (defined by Bennett et al., 2022). The Knockfarril Hill (Fedo et al., 2020, this issue; Caravaca et al., 2022) and the Glasgow members of the C.Shoemaker formation are located in this area.

The Siccar Point group unconformably overlies the Mount Sharp group, and contains the Stimson formation (Banham et al., 2018, 2020), and other unnamed (and untraversed) mantling units that outcrop along the north flank of Aeolis Mons (Anderson & Bell, 2010). The unconformity separating these two groups is referred to as the Base Siccar Point group unconformity. The Stimson formation is a decameter-thick unit composed of aeolian sandstones, that mantles an inclined deflational unconformity (Banham et al., 2018; Watkins et al., 2016, 2022). A more detailed description of the stratigraphic relationships of the Stimson formation is provided later. The Stimson formation has been traversed and identified at four geographically distinct areas: Emerson plateau (Sol 992–1154); Naukluft plateau (Sol 1276–1353); Murray buttes (Sol 1383–1455) and the Greenheugh pediment (Sol 2665–2734) (Figure 1a).

The Greenheugh pediment is an erosional unconformity which is an up-slope extension of the base Siccar Point group unconformity. The unconformity is capped by a fan-shaped sandstone body which radiates from the Gediz Vallis canyon. The fan shaped body is an erosional feature and is bordered by steep edge of about 10 m revealing a typical thickness of a few meters overlying Mount Sharp group strata, and covers an area of 2.66 km^2. Certainty of the thickness of the unit diminishes toward the interior, due to an absence of rover data. Using the rover, the MSL team investigated the northern margin of the Greenheugh pediment capping unit. Here it is expressed as a gray-colored, resistant, cliff-forming unit that overlies the Glasgow member of the C.Shoemaker formation.

3. Data and Methods

3.1. Instruments

Facies and architectural information came from photomosaics constructed from images acquired by the Navigation cameras (Navcam: Maki et al., 2012) and the Mast cameras (Mastcams: Bell et al., 2017). Both of these instruments are mounted on a pan-tilt unit fixed atop of the Remote Sensing Mast, ~1.9 m above the surface (Warner et al., 2016). Context, image targeting, and quantitative stereo meshes were facilitated through stereo Navcam data. The Mastcams (Left = 34 mm, right = 100 mm focal length) were used primarily to image outcrops for the purpose of scientific investigation.

Sedimentary texture, and grain size measurement information were collected using the Mars Hand Lens Imager (MAHLI) on the instrument cluster on the end of Curiosity's robotic arm (Edgett et al., 2012). At highest resolution, MAHLI can collect images with 14 μm/px, at a working distance of 21 mm (Edgett et al., 2012), typically

collected as a series of nested images with granularities of 16–21 μm/pixel, 31 μm/pixel, and 100 μm/pixel, at working distances of ~20, 50, and 150 mm (Yingst et al., 2016). Coverage of MAHLI images obtained are depended on mission cadence, and stability of the rover, time available (arm deployment is a two sol process), and other constrains described by Yingst et al. (2016).

Satellite-derived orthomosaics were used as a base map for determining the rover's location, and for photogeologic mapping. Data was provided by the High Resolution Imaging Science Experiment (HiRISE; McEwen et al., 2007) aboard the Mars Reconnaissance Orbiter (MRO), and the Mars Orbital Laser Altimeter (MOLA; Smith et al., 2001) aboard the Mars Global Surveyor (MGS). A composite photomosaic, and digital elevation map (DEM) of the MSL field site was assembled by Calef and Parker (2016), which was tied to the absolute elevation derived from the MOLA elevation model.

3.2. Data Collection

As shown in Figure 1b, Curiosity embarked on a science campaign to investigate the pediment capping unit between Sols 2618 (18 December 2019), and 2780 (1 June 2020). Images of the pediment capping unit were collected from a vantage point at Western butte before the rover traversed onto the pediment around Sol 2695. Geochemical data pertaining to the capping unit were collected using the ChemCam and APXS instrument as the rover traversed the pediment capping unit. Drill tailings from the Edinburgh drill site, (Sol 2702 end-of-drive location) were analyzed by the SAM instrument suite. These geochemical data are described in detail by Bedford, Banham, et al. (2020), Bedford, Schwenzer, et al. (2020) and Thomson et al. (2011).

3.3. Nomenclature

The International Astronomical Union (IAU) determines formal names of features identified on Mars. Within this paper, Earth, Mars, Gale, Aeolis Mons, Aeolis Palus and Gediz Vallis are the only features formally designated by the IAU. All other features and targets were informally named by the MSL team during surface operations in a scheme described by Vasavada et al. (2014). The landforms Tower, Central, and Western butte are defined in the overview paper (Bennett et al., 2022). Mars also has no internationally recognised formal stratigraphic code, and so, all geologic units are informal. Stratigraphic units (e.g., formation, member, bed, etc.) should be recorded in lowercase letters, in accordance to the North American Stratigraphic Code (NACSN, 2005), and as implemented by the United States Geological Survey writing-style (Hanson, 1991), or British Geological Survey classification of lithodemic units (Gillespie et al., 2008).

3.4. Terminology for Cross-Strata

In this contribution, a “cross-set” or “set of cross-strata” is defined as a package of cross-laminations that were deposited by the same migrating bedform (sensu McKee & Weir, 1953). Each cross-set is composed of a package of cross-laminations, encapsulated by a lower bounding surface related to the overlying cross-strata, and an overlying bounding surface related to the overlying cross set.

In the pediment capping unit, both simple and compound cross-sets have been identified, in which set-bounding surfaces can have slightly different names. Where simple cross-sets are observed, sub-horizontal bounding surfaces defining the base of a cross-set can be described as a set bounding surface. Other valid terms include: first-order surfaces (Brookfield, 1977); interdune surfaces (Kocurek, 1981); and dune bounding surfaces (Banham et al., 2018). Where compound cross-sets (cosets) are identified, the basal sub-horizontal bounding surface is given the term compound-set bounding-surface (sensu Banham et al., 2021). Compound cross-sets contain internal erosion surfaces, given the descriptive term subset bounding surfaces (sensu Rubin & Hunter, 1983). These can be formed by two common processes: changes in dimension or direction of a dune by reversal of flow (third-order surfaces; Brookfield, 1977) or dynamic interaction of contemporaneous dunes (Brothers et al., 2017); or by migration of a scour trough preceding a superimposed dune (second-order surface, Brookfield, 1977; Kocurek, 1991). Despite their similar appearance, they can be differentiated by viewing the three-dimensional relationships with other bounding surfaces and cross-strata (Rubin, 1987; Rubin & Hunter, 1983).

3.5. Data Analysis

Analysis of image data (Navcam, Mastcam, MAHLI, and HiRISE products) was performed using standard photogeology interpretation methods (De Hon et al., 2001; Moore, 1971; Nesbit et al., 2020), and using previous approaches used studying the Stimson formation and the basal unconformity (Banham et al., 2018, 2021; Watkins et al., 2016, 2022).

Images collected by the rover underwent radiometric calibration, white balance, and geometric calibration before interpretation (Bell et al., 2017). Navcam and Mastcam images were mosaiced with geometric adjustments to preserve relations. Using methods described by Alexander et al. (2006), a terrain mesh was generated from Navcam stereopairs for measurement of geologic features. Corrected images and mosaics were then interpreted using vector graphics software to highlight outcrop architecture and depositional features.

Visual estimation of cross-bed dip azimuth was performed as part of this study, particularly for outlying outcrops beyond the limits where digital outcrop models (DOMs) can be reliably constructed (>40 m), or where stereo Mastcam data was not available. Details of this method can be found in the SI material, and in Banham et al. (2021); Banham et al. (2018).

Textured three-dimensional DOMs were generated using Mastcam stereo images using the Planetary Robotics Vision Processing tool (PRoViP) (Paar et al., 2012), and were interpreted using Planetary Robotics 3D viewer (PRo3D) (Paar & Consortium, 2016; Traxler et al., 2018). Where DOMs exist, this software was used to measure geometric attributes of the sedimentary architecture, including set thickness, and dip-azimuth of cross-laminations, and subset bounding surfaces. Barnes et al. (2018) provides a comprehensive description of methods used.

4. Results and Interpretation

4.1. Regional Stratigraphic Relationships of the Stimson Formation

This section will discuss the regional-scale relationship of the Stimson formation, and the capping unit at the Greenheugh pediment. The profile of the underlying unconformity, the thickness of the unit (based on surface and orbital measurements), and the underlying C.Shoemaker formation will also be discussed.

At the time of writing, all outcrops of Stimson formation observed along the traverse superposed various units of the Mount Sharp group, where the erosion-resistant, gray, cross-bedded sandstones of the Stimson formation are juxtaposed above the smooth-weathering, tan-colored, laminated and fractured rocks of the Mount Sharp group. Separating these two units is the base Siccar Point group unconformity. The Stimson formation and Mount Sharp group strata are still in their original depositional orientation–apparently near horizontal when viewed perpendicular to the regional dip (Stein et al., 2020). The unconformity cross-cuts the bedding of the Murray and C.Shoemaker formations defining a disconformity-type unconformity. This boundary has been mapped at the interface of these two units along the present extent of the traverse (Figure 3) (Watkins et al., 2022).

In Stimson outcrops on lower Aeolis Mons (Figure 1: Emerson, Naukluft & Murray buttes), the Stimson formation overlies the Pahrump Hills, Hartmann's Valley and Karasburg members of the Murray formation. On the northern margin of the Emerson plateau, by Marias Pass, the Stimson formation overlies the Pahrump Hills member, and is up to 6 m thick (Banham et al., 2018). The unconformity rises by ~25 m toward the south of Emerson plateau, where the Stimson formation at East Glacier is observed to be 6m thick (Banham et al., 2018). At the Naukluft plateau, the Stimson overlies the Hartmann's Valley member, and ranges in thickness between 2 m on the east side, to ~8 m on the west side by Hartmann's valley (Bedford, Schwenzer, et al., 2020). At the Murray buttes, the Stimson overlies the top-most part of the Hartmann's valley member and the lower-most Karasburg member, and the buttes typically range between 5 and 12 m thickness. The unconformity rises by approximately 40 m of elevation from the north to the south of the buttes over a distance of ~600 m. Onlap onto the unconformity can be observed at the base of Butte M1b (Banham et al., 2021).

Across the section of Aeolis Mons traversed by the rover, the Stimson sandstones superposes a vertical succession of ~140 m of the Mount Sharp group, over a north-south profile of 1.7 km (Figure 3). Locally, the unconformity records palaeotopography–ranging from a few centimeters at Missoula (where there are rip-up clasts incorporated into the basal Stimson cross-sets), up to ~7 m at Logan's run, and 3 m at Butte M1b (Banham et al., 2018).

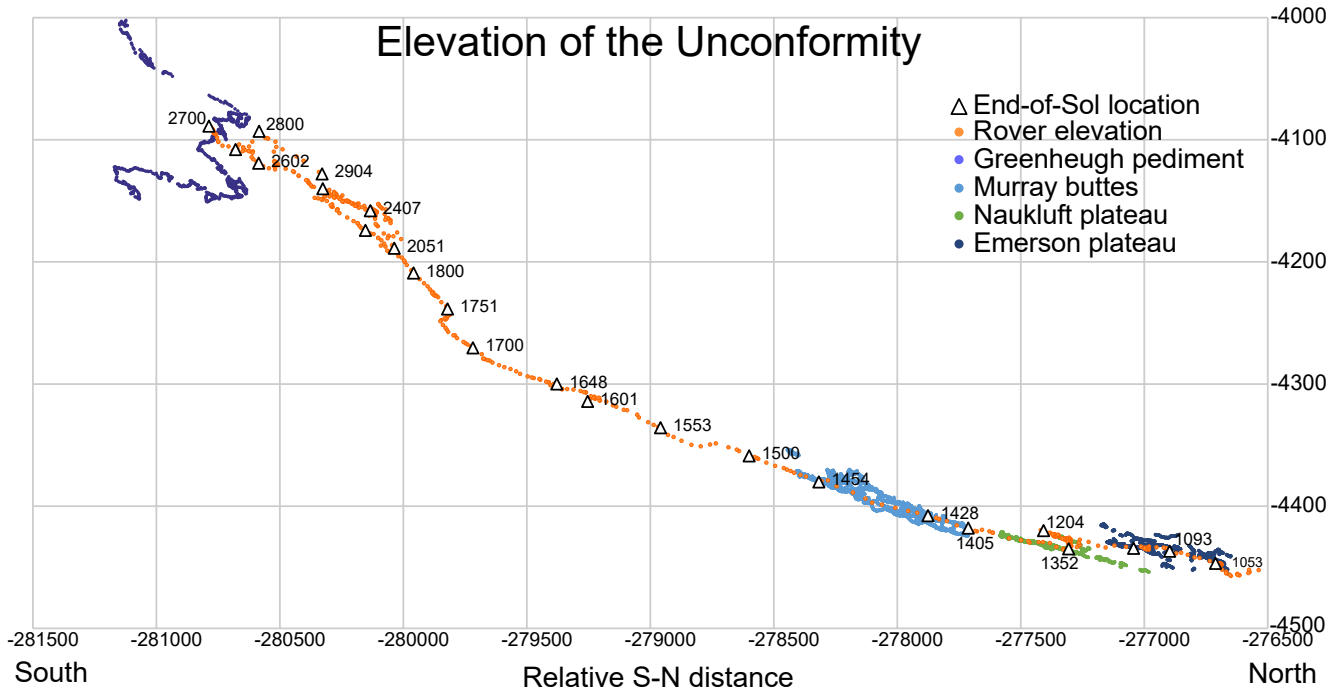

Figure 3. Elevation of the base Siccar Point group unconformity (base Stimson unconformity), from the north margin of the Naukluft plateau, to the south margin of the Greenheugh pediment. The orange points denote the elevation of the rover along the traverse, with the blue, green and purple points indicate the elevation of the unconformity observed at the base of the Stimson formation, as observed from the rover using the Mastcam instrument. Triangles indicate the end-of-Sol rover locations.

There is a 2.5 km expanse between the southern edge of the Murray buttes and the northern margin of the Greenheugh pediment within which outcrops of Stimson formation are largely absent. A few isolated outcrops exist which may have an association to the Stimson formation, including Lobster Mountain, Pile Mountain, and Ireson Hill. In the 2.5 km between outcrops, the elevation of the unconformity increases by over 200 m, from −4,375 to −4,150 m. Mapping of the unconformity around the Greenheugh pediment using HiRISE orthomosaics records an elevation change of ∼250 m along a 1.5 km north-south profile. At the Greenheugh pediment, the capping unit is interpreted to overlie the Glasgow member of the C.Shoemaker formation at its northern margin and unmapped units higher in stratigraphy to the south and the Glasgow member of the C.Shoemaker formation (Figures 1 and 2). From orbital mapping, the lowest point of the unconformity is on the northwest side of the pediment, at approximately −4,150 m. The highest points are mapped on the east side of the pediment where the height of the base of the pediment is between −4,000 m and −3,900 m. An isopach map interpolated from HiRISE data of the unconformity suggests that the pediment is plausibly between 2 and 12 m thick (see Text S1 in Supporting Information S1). The study area thickness is predicted to be between 2 and 5 m, with the thickest parts of the pediment predicted on the west flank of the pediment.

4.2. Subdivision of the Stratigraphy at the Greenheugh Pediment

Within the study area, the Stimson formation can be subdivided into three main intervals based on stratigraphic architecture and foreset dip-azimuth of cross-laminations. Each interval is summarized as follows: the basal Gleann Beag interval is characterized by compound cross-bedding and northeast cross-set dip-azimuths; the middle Ladder interval, is characterized by simple planar cross-sets and southward cross-bed dip-azimuths; and the Edinburgh interval, at the top of the section where the Edinburgh drill site is located, is characterized by simple trough cross-bedding and westward dip-azimuths. For context, the spatial distribution of these intervals are shown in Figure 4, plus in three high-resolution full mosaics available online, and in the JGR-P supporting information. URL links to these high-resolution mosaics are provided in the figure captions. The justification for these subdivisions will be further explained in the stratigraphic architecture section.

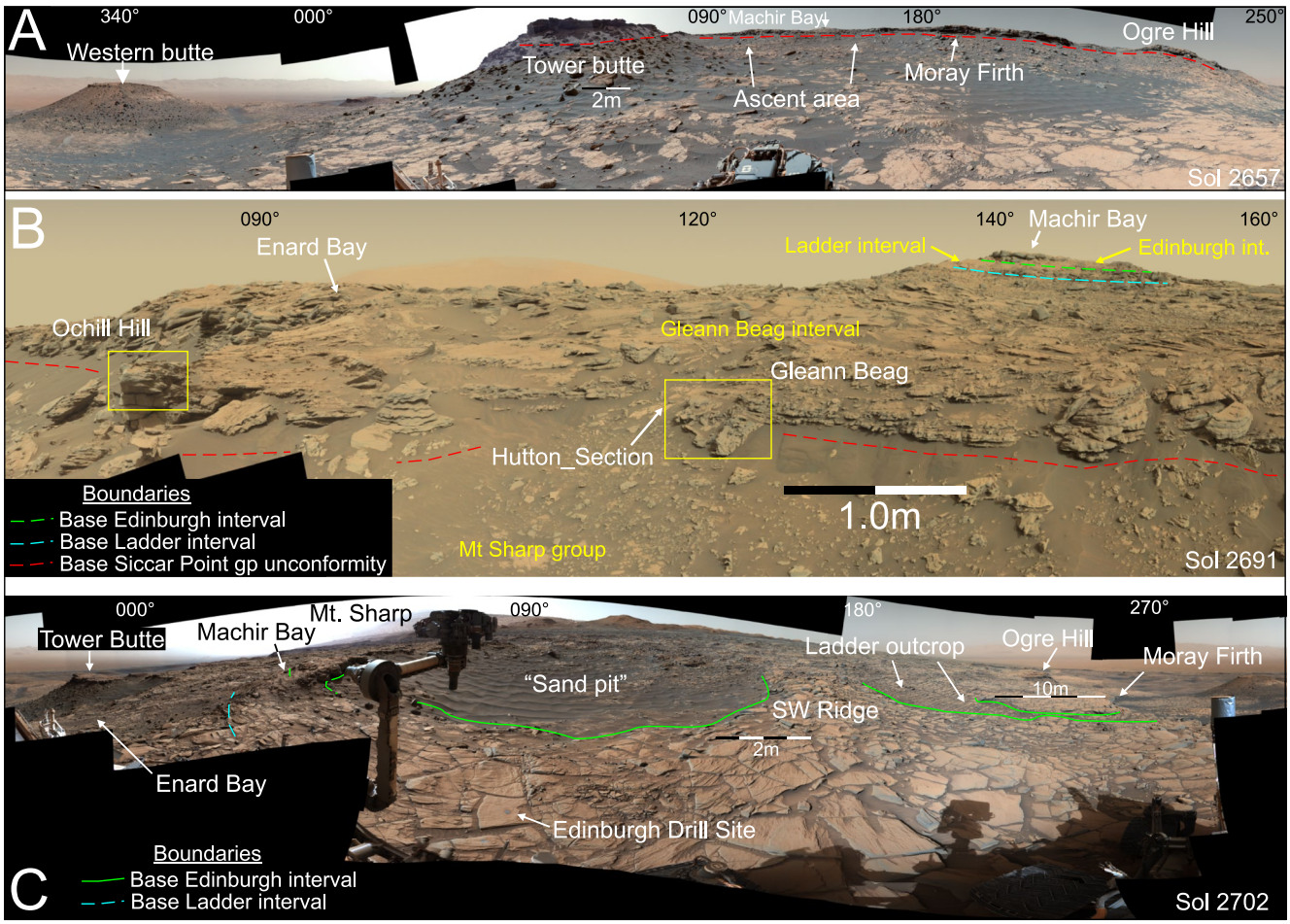

Figure 4. Context images to show spatial relationship between key outcrops observed at the Greenheugh pediment study area. High-resolution versions of these images are available by clicking on hyperlinks. See Figure 1b for orthomosaic depicting location of key outcrops. (a) Mastcam 360° mosaic taken from the foot of the pediment capping unit. High-resolution panoramic image of 4A (Mastcam mosaic ML_mcam13911, acquired on Sol 2658, at Sol 2657 end-of-drive location). (b) Pediment ascent area. Mosaic depicts outcrops and targets near where the rover drove onto the Stimson formation. High-resolution image of 4B (M100 Mastcam mosaic MR_mcam014078, acquired on Sol 2691, at Sol 2691 end-of-drive location). (c) Mastcam 350 mosaic taken at the Edinburgh drill site on top of the pediment capping Stimson formation. Green lines delineate the stratigraphic boundary between the Ladder interval, and the upper Edinburgh interval. High-resolution panoramic image of 4C (M34 mosaic ML_mcam014196, acquired on Sol 2711, at Sol 2702 end-of-drive location). Image credit: NASA/JPL-Caltech/MSSS.

At the time of this study, the term stratigraphic "intervals" were chosen to describe these units, due to their observed limited lateral extent of a few hundred meters on the north margin of the pediment. If these intervals can be correlated to other stratigraphic sections, they can be updated to "member" status. In this section, we examine the outcrop architecture and the relationship of each of the intervals, to understand the bedform dynamics which gave rise to the different stratigraphic architectures.

5. Sedimentary Textures and Depositional Processes

The sedimentary texture and facies of the pediment capping unit provide constraints on depositional origin.

5.1. Sedimentary Texture

The rover traversed onto the pediment capping unit between Sols 2693 and 2734, which enabled investigation of its sedimentary texture using the MAHLI, and Mastcam instruments. In total, MAHLI was used to investigate 14 rock targets, six of which were suitable for grainsize analysis. A qualitative description of the grain size and texture is provided, along with a quantitative measurement of grain size and sorting. The three superposed

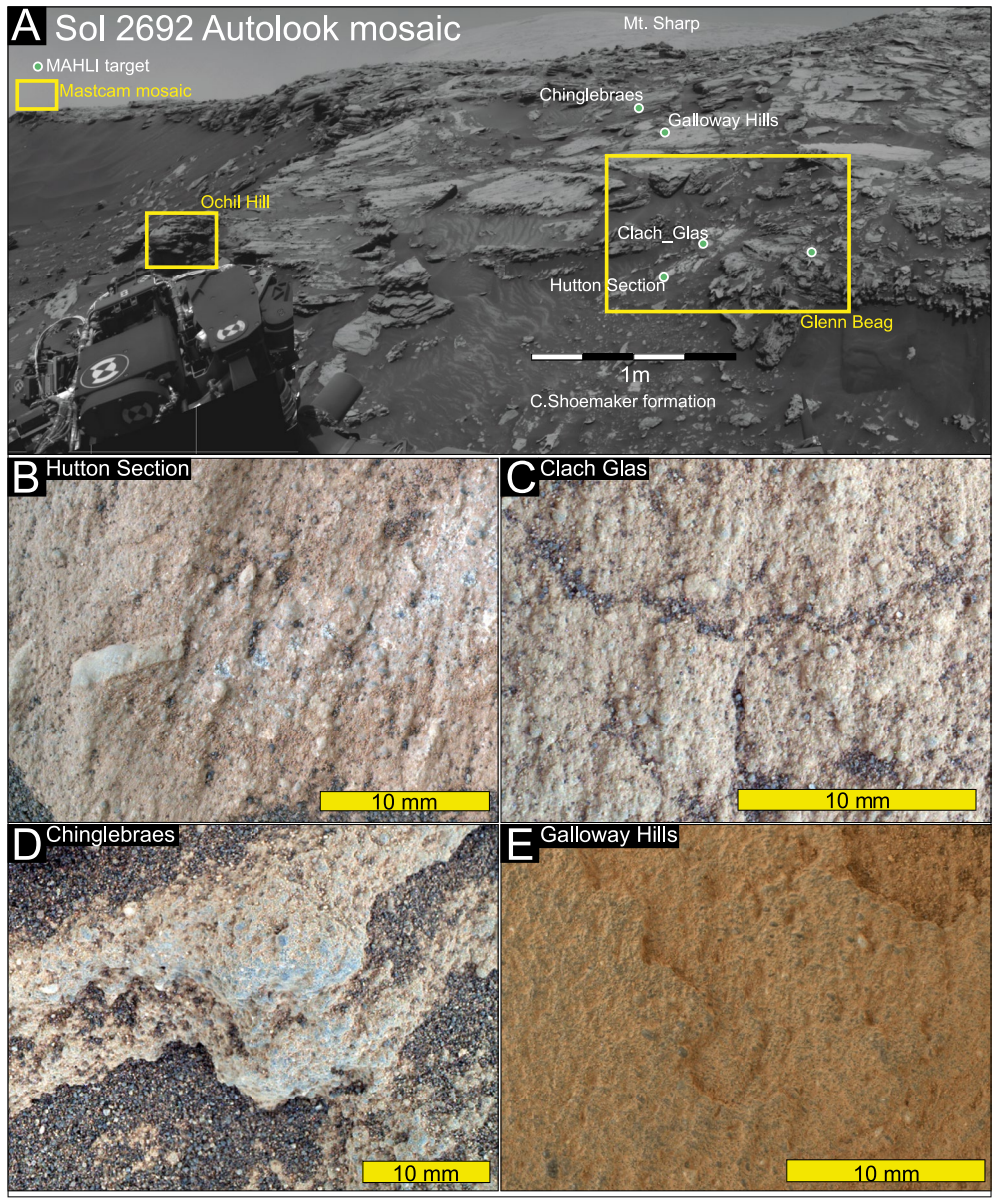

Figure 5. Mars Hand Lens Imager (MAHLI) images taken from near the unconformity, showing sedimentary texture. (a) Overview Navcam mosaic showing basal section of the pediment capping unit, and location of key MAHLI and Mastcam targets. High-resolution panoramic version of 5A. Sol 2692 end-of-drive Navcam mosaic. (b) Hutton Section, 5 cm stand-off. Target was located just above the unconformity and contains large clasts that are interpreted to be derived from the (c) Shoemaker formation. ChemCam LIBS shots are visible in this image. (c) Clach Glas target, 5 m stand-off. Prominent well-rounded grains are visible in this target. (d) Chinglebraes target, part of the MAHLI dogs-eye mosaic. Dark grains observed in this mosaic are superficial sand grains perched on laminations. (e) Galloway hills target, 5 cm stand-off. This image is a planform image of the upper surface of a lamination. Image credit: NASA/JPL-Caltech/MSSS.

stratigraphic intervals are mentioned in this section, but will be discussed in the stratigraphy and stratigraphic architecture section.

5.1.1. Description

In general, the capping unit is characterized by sandstones, which are composed of medium-grained, well-sorted, sub-to well-rounded, sub-spherical grains (Figure 5). Detrital grains are gray in color, with an increased number of cream or tan-colored grains toward the base of the section, where extraformational clasts are present. Bimodal

sorting is observed throughout the succession, at various targets. Some concretions were observed where differential weathering had caused them to weather-out of the outcrop.

The basal Gleann Beag interval is recorded in 5 MAHLI targets. In the lower section, grains are variable in color–being gray or cream–and are slightly more poorly sorted than the rest of the capping unit. Prominent cream-colored grains (~2% of grains at Chinglebraes) show grain-sizes of 0.2–1.0 mm diameter and are relatively well rounded. Grains typically have a smooth surface; however, some examples were pitted. One large angular clast measuring 10 mm in length is observed at Hutton's Section. Gray grains are typically smaller in size, centering on medium-grain. There are sporadic black grains observed too. Targets such as Clach_Glas and Chinglebraes exhibited bimodal sorting (Figure 5). At Chinglebraes (Figure 5a), wind ripple laminations 2–4 mm thick were traced laterally for 0.8 m distance. Mastcam data provide additional insight into sedimentary texture and the processes that occurred immediately above the unconformity (Figure 4a), at the Hutton's section (Sol 2694), Glenn Beag (Sol 2695) and Ochil hill (Sol 2694) targets. At Glenn Beag large (~1 mm) white colored grains are observed interspersed with other smaller grains, accounting for approximately 2% of the total grains. The largest of these grains were observed to be more angular, and irregular in shape. At Ochil Hill, similar, white-colored grains were identified both in lags (at the base of the outcrop), and throughout the outcrop.

The central Ladder interval (Figure 4) is recorded by the Forsinard flows target at the Machir Bay outcrop. Concretions measuring between 5 and 20 mm in diameter are present, and are composed of well-cemented sands grains. The concretions are distributed randomly, but evenly across the face of the sandstone block. Close inspection of the concretions indicates that pore spaces between grains may consist of amorphous white material. Across the target, where grains weather proud of the surface, they are well-rounded with relatively smooth surfaces. Some grains do exhibit slight surface pitting.

The uppermost Edinburgh interval (Figure 4c) was characterized by the Assynt Window target that records a weathered section cross-cutting several cross-laminations. An oblique section through the laminations revealed subtle changes in grainsize through the laminations. The upper part of the laminations is characterized by flat-weathering sections composed of larger grains roughly 0.7–0.8 mm in size, that are well rounded. Immediately beneath these prominent layers is a recessive layer that forms a step, and is composed of apparently slightly finer sand particles, where grains are more difficult to define. This is then followed by a more proud-weathering layer of larger sand grains.

5.1.2. Grainsize and Sorting Analysis Using MAHLI Data

Grain-size analysis was performed on 9 MAHLI images, where sufficient grains could be identified uniformly across the image. Analysis was conducted using the same methodology as Banham et al. (2018) at Emerson plateau. In total 1950 grains were measured across all the samples, with analysis being performed on all measured grains as well as grains from individual images. The whole sample set indicates that the pediment consists of a bimodal, moderately well-sorted, medium-grained sandstone, with a geometric mean grain size of 486 μm, a sorting of 1.499, with a symmetric skewness. The geometric mean grain size for individual samples range between 335 μm for Galloway Hills, and 634 μm at Assynt Window. Details for each target are provided in Text S1 in Supporting Information S1.

5.1.3. Interpretation

The grain size distribution, sorting and roundness observed are characteristic of wind-blown sediments. Bimodal sorting is frequently observed in aeolian sediments, where saltating particles facilitate the movement of larger grains via surface creep (Greeley & Iversen, 1985; Jerolmack et al., 2006). Grains throughout this study area (with the exception of C.Shoemaker formation rip-up clasts) are sub-to well-rounded, which is characteristic of grains moved by the air, where impacts quickly round the grains (Garzanti, 2017; Garzanti et al., 2015; Kuenen, 1960). In some targets, particularly at Adder and Assynt window targets, there are layers of coarser grains observed to overlie finer-grained laminations (where grains are not resolved). This is consistent with inverse grading, a commonly observed phenomenon in wind-ripple laminations–or pinstripe laminations–where the airflow sorts the grains into laminations with inverse grading (Fryberger & Schenk, 1988).

White-colored grains observed using the Mastcam at Hutton_section and Clach_Glas are interpreted to be C.Shoemaker formation rip-up clasts that have been reworked into the basal section of the Stimson formation. Although the chemical composition of the grains cannot be used to verify the origin of these grains (no grains

were sampled using the ChemCam instrument), they are visually similar to C.Shoemaker formation observed immediately beneath the unconformity. The MAHLI image taken at the Hutton's section adds further evidence to support this, where large angular clasts composed of material akin to the C.Shoemaker formation are observed. This would not be the first observation of the Mount Sharp group being reworked and incorporated into the Stimson formation. Murray formation rip-up clasts have been observed at the Emerson plateau, at the Missoula and Lumpry targets in Marias Pass (Banham et al., 2018). Similar white-colored grains are also seen in the Bagnold dunes (Ewing et al., 2017).

5.2. Sedimentary Structures

To reconstruct the sedimentary processes, occurring during the accumulation of the strata, commonly observed lithofacies are described here. Additional lithofacies description for other areas of the Stimson formation are provided for: the Emerson plateau (Banham et al., 2018); the Naukluft plateau (Bedford, Banham, et al., 2020); and the Murray buttes (Banham et al., 2020). Four facies have been identified, each characterized by unique sedimentary structures (Figure 5).

5.2.1. Wind-Ripple Strata

Description: The dominant stratification type identified in the Stimson formation are plane-parallel laminations that have uniform thickness and are highly laterally persistent. The best example of these are observed at the Enard Bay outcrop (Figures 5b and 5b'), where trough cross-sets are composed of laminations with a uniform thickness of between 2 and 4 mm, and lateral persistence in excess of 1.2 m (Figure 5c). The laminations exhibit a uniform thickness along their length from the top right of the outcrop adjacent to their upper bounding surface, down to the lowest visible part of the set, where the cross-laminations appear to curve to become more horizontal. This slight curvature is related to their position within the trough cross-set. Closer inspection of the cross-laminations (Figure 5b') indicate that each lamination has a more prominent erosion-resistant component, adjacent to a less prominent recessive component.

Interpretation: Wind-ripple laminations with uniform-thickness are interpreted as translatent wind ripple strata (Hunter, 1977). Each of these laminations represents the migration of a single millimeter-high ripple migrating in a down-wind direction (Fryberger & Schenk, 1988). The prominent and recessive layering may be a visual expression of grainsize differences within each lamination. This may relate to inverse grading which occurs as a result of finer particles being trapped and preserved by coarser, less transportable grains accumulating as the ripples migrate downwind (Fryberger & Schenk, 1988). These ripples occur commonly on the stoss side of dunes, and on dune lee faces that are oblique to the wind (Eastwood et al., 2012).

5.2.2. Avalanche Deposits

Description: Avalanche deposits were observed in association with planar cross-sets observed in the Ladder section (Figure 5c). Here, a simple laterally extensive planar cross-set shows alternating packages of two distinctive layer types: (a) well-defined thin, weathering-resistant laminated layers; (b) thicker layers with less well-defined internal structure (Figure 5c'). The thicker layers commonly contain diffuse and poorly defined wedge-shaped geometries that pinch out parallel to strike (marked AV, Figure 5c').

Interpretation: The thicker, less resistant depositional packages are interpreted to be avalanche strata (also commonly called grainflow strata), formed by sand avalanching down the lee face of a dune (Hunter, 1977; Kocurek & Dott, 1981; McDonald & Anderson, 1995; Nield et al., 2017). We interpret the avalanche strata from the presence of wedge-shaped depositional packages, which are typically much thicker than adjacent wind ripple strata (Hunter, 1977). Frequent avalanches across the width of the lee slope cause laterally discrete grainflows to amalgamate into a single package spanning much of the width of the lee slope (Hunter, 1977). These packages show little internal structure (at a distance) due to poor grain packing during grainflow (Lindquist, 1988). Avalanche strata typically occur on dunes in areas where the slip face is perpendicular to the wind (Eastwood et al., 2012). The prominent-weathering thin laminae that surround the grainflow strata are interpreted to be wind-ripple strata formed by reworking of grainflow beds by wind-ripples migrating obliquely along the lee face.

5.2.3. Trough and Planar Cross-Bedding

Description: Cross-bedding is the most ubiquitously identifiable sedimentary structure found within the Stimson formation. An example selected from Tower butte is shown in Figure 5a. Cross-sets are largely composed of dipping millimeter-thick uniform and persistent laminations (interpreted to be wind ripple strata), which characteristically curve asymptotically down onto a basal bounding surface. The uppermost part of the laminations are truncated by a bounding surface associated with an overlying cross-set. The basal bounding surface are planar in sections perpendicular to the dip of the cross-laminations, or trough-shaped in sections parallel to strike. Bounding surfaces can dip at several degrees or appear to be sub-horizontal. Cross-sets across this study area have typical thickness ranges of 0.3–0.8 m. Where trough-crossbedding is identified, troughs have measured widths ranging between 1.5 and 4 m. Where cross-sets appear to be planar, lamina-sets can be traced parallel to strike for distances of between 3 and 50 m.

Interpretation: Cross-stratification in the Stimson formation is interpreted to represent deposition from the migration of aeolian bedforms. Dipping cross-laminations are interpreted to represent the preserved lower section of the dune, which downlap onto a scour surface formed by a scour trough that migrates in advance of the dune lee as the dune migrates. Cross-laminations (including avalanche strata, where present) represent the incremental accumulation of sediment transported by various mechanisms on the lee slope of the dune as the dune migrates. Inclined and sub-horizontal bounding surfaces represent erosive surfaces formed by different mechanisms related to dune migration. Inclined bounding surfaces, referred to as subset bounding surfaces (Hunter & Rubin, 1983; Rubin & Hunter, 1983) can be associated with migration of superimposed bedforms down or oblique to the lee of a primary dune (Rubin & Hunter, 1983; second-order surface – Brookfield, 1977; Superposition surface – Kocurek, 1991; Rubin & Carter, 2006). Alternatively subset bounding surfaces can form by fluctuating or reversal of flow (Hunter & Rubin, 1983; third-order surface – Brookfield, 1977; reactivation surface – Kocurek, 1991). Sub-horizontal bounding surfaces are the time-translatent scour surface formed by a scour trough preceding a primary dune as it migrates. These surfaces can either be simple-set bounding-surface, where the overlying cross-set is simple, or a compound-set bounding-surface where the overlying cross-set contains compound cross-bedding (sensu Banham et al., 2020).

5.2.4. Concretion-Rich Sandstone

Description: This facies consist of cross-bedded sandstone that contain abundant spheroidal concretions. From a distance, these facies appear to have a lumpy or knobbly surface texture, and are typically associated with the strata immediately above the basal unconformity. Concretions become progressively less common with increasing stratigraphic height above the unconformity. In cross-sets immediately above the unconformity, concretions can be pervasive, and densely packed enough to be amalgamated. Typical concretions are sub-rounded to oblate in shape and have diameters ranging between 10 and 40 mm. Sand grains are observed protruding from within concretions, along with undeformed laminations that are concordant to primary deposition packages within the host cross-sets.

Interpretation: Concretions form as a result of diagenesis within the subsurface, where chemical precipitates accumulate onto a nucleation point within the host rock. The cementing agent encrusts the grains surrounding the nucleation point, and the concretion grows by pervasive growth through the pore spaces surrounding adjacent grains. This allows the concretion to grow without deforming the original depositional structures seen across the pediment. This cementing agent could be derived from a slow-flowing chemically saturated pore-fluid (Berner, 1968), and can have slow growth rates (Wilkinson & Dampier, 1990). The preferential distribution of concretions toward the base of the Stimson formation, coincides with a prevalence of ripped-up and incorporated material from the underlying C.Shoemaker formation in the base of the Stimson formation. It is possible that the particles acting as the nucleation points could be derived from the C.Shoemaker formation.

6. Stratigraphic Architecture

Within the study area, the Stimson formation is subdivided into three distinct stratigraphic intervals, based on their sedimentary architecture and palaeotransport direction. This section examines the outcrop architecture and relationship to each other, to understand geomorphic processes that gave rise to the different stratigraphic architectures. For context of, the reader is referred to Figure 4 and the associated high-resolution mosaics which show

the spatial relationships between key outcrop locations across the study area. URL links to these high-resolution mosaics are provided in the figure captions.

More comprehensive descriptions of outcrops mentioned in this study are provided in the directory of outcrops provided in Text S1 in Supporting Information S1.

6.1. Gleann Beag Interval–Compound Dunes

The basal unit of the Stimson formation in this study area is informally named the Gleann Beag interval. It has a variable thickness, ranging between 3.6 m at Hutton's section (where the rover ascended the pediment), thinning to ∼1 m eastwards at the Moray Firth outcrop, and apparently pinching out before the Ogre Hill outcrop (Figure 1b).

General Description: The Gleann Beag interval is exposed in the Tower butte cap, the pediment ascent area up to the base of the Machir bay outcrop, and east across to the lower section of the Moray Firth outcrop. Tower butte (Figure 7a), is composed of compound cross-bedded sandstones, in which a coset 2 m thick can be observed. Compound cross-bedding is composed of smaller scale cross-sets (termed subsets) with thicknesses between 0.3 and 0.8 m, and are bounded by inclined subset bounding surfaces. In Figure 5a, cross-laminations within the subsets, commonly have an apparent dip toward the east at ∼5° (left of the image). The inclined subset bounding surfaces, have an apparent dip to the west. The uppermost set shows cross-laminations which are inclined to the west with an apparent dip of ∼10° (Figures 7b and 7c). The west face of Tower butte (Figure 6a) exhibits a similar array of compound cross-sets with subset thicknesses of between 0.3 and 0.5 m. On the west facing side, cross-laminations and subset bounding surface dip north. The apparent dips from the north- and west-facing sides yield an average true cross-lamination dip-azimuth of 17° toward 027° and a subset bounding surface dip-azimuth of 12° toward 321°.

South of Tower butte, in the area where the rover traversed onto the pediment capping unit (Figures 4a, and 4b–ascent area), the Gleann Beag interval was observed at close proximity (Figures 4b and 5a). The Gleann Beag target (Figures 4b, 5a, 8c and 8c') is in the lower part of the capping unit stratigraphy, no more than a meter above the basal unconformity. Observations using Mastcam and MAHLI recorded cross-bedded sandstones characterized by laterally persistent, uniform-thickness cross-laminations. Close inspection of Mastcam images reveal some coarse-grained material ranging between coarse-sand to small-pebbles in size (Figure 8c'). Many of the resolvable coarse sand grains are white, similar to those seen in MAHLI images of this outcrop (Figure 4). There are some rare, well-polished, subangular to well-rounded pebbles in the lower-most part of the section. These clasts range from nearly spherical to sharp-edged angular grains (Figure 8c'). Concretions are common in this section, although they are isolated, and seldom coalesce.

Laterally, at the Ochil Hill outcrop (Figures 8a and 8b), trough cross-bedded sandstones composed of wind-ripple laminations are observed, with sets approximately 20 cm thick. The lower two cross-sets exhibit a rougher surface texture and are composed of wind-ripple laminations. The sand grains are predominantly gray, however 5%–10% of the grains are white colored. Above these two sets, there is a single large trough cross-set with sparse white grains, and a smoother surface texture. The axes of the troughs here are aligned broadly toward the northwest. Measurement of cross-lamination dip azimuths using a DOM indicate a dominant dip direction toward 061°.

Higher within this interval, at the Enard Bay location (Figures 4b and 6b), an intersection between two troughs–a bounding surface–can be identified, with the trend oriented broadly northeast-southwest. The northern trough (left of image) is composed of cross-laminations, which are parallel and uniform in thickness (Figures 6b and 6b'). From the truncation surface, these laminations curve downward, progressing toward horizontal at the edge of the pediment (toward the left of the image), with a preserved partial width of 2.5 m. Cross-lamination dip-azimuths of the troughs were measured using a DOM. The dip azimuths of the two adjacent sides of the trough gave a bimodal dip azimuth trend: a dominant trend toward the north, and another toward the southeast. The bisecting angle, which gives the resultant dip-azimuth trend of the trough cross-sets is toward 052°. The bounding surface between the two trough cross-sets dips toward the southeast, with a dip-azimuth of 057°.

The Moray Firth outcrop–to the west of the ascent area–exposes the boundary between the Gleann Beag and Ladder intervals (Figures 4a and 9a). The outcrop can be broken into two distinct sections–a lower nodular

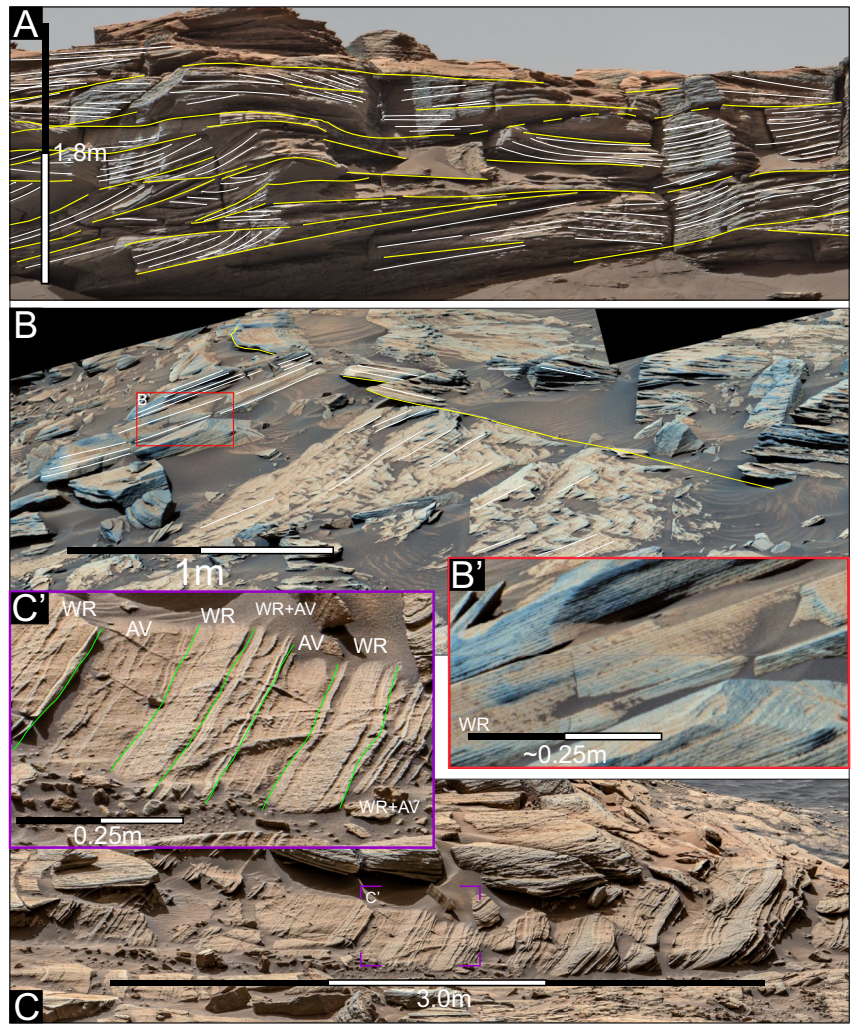

Figure 6. Representative example of Stimson formation facies observed at the Greenheugh study area. (a) Trough cross-bedding observed in the west-facing cliff of Tower butte. Cross-laminations (white) and bounding surfaces (yellow) are highlighted to show geometric relationships. High-resolution image of 6A (M100 mosaic MR_mcam13916, acquired on Sol 2658, at Sol 2657 end-of-drive location). (b) Trough cross-bedding observed at Enard Bay. The bounding surface (yellow) scours the lower left trough cross-set and defines the lower boundary of the cross-set on the right side of the image. High-resolution image of 6B (b') Close-up image of pinstripe laminations observed in part (b) Here, laminations can be traced laterally for distances in excess of 1 m. (M100 mosaic MR_mcam14115, acquired on Sol 2697, at Sol 2695 end-of-drive location) (c) Planar cross-laminations observed at the Ladder outcrop. Here windripple laminations and avalanche strata are contained within a planar, tabular shaped cross-set. See Figure 10a for more context. (M100 Mastcam mosaic MR_mcam14303, acquired on Sol 2729, at Sol 2702 end-of-drive location). (c') Close-up images of Ladder section, showing interstratified windripple strata (WR–resistant and well laminated), and avalanche strata (AV–recessive, "wispy" laminations). High-resolution image of 6C, including 6C' (M100 Mastcam mosaic MR_mcam14303, acquired on Sol 2729, at Sol 2702 end-of-drive location). Image credit: NASA/JPL-Caltech/MSSS.

recessive-weathering section, which forms part of the Gleann Beag interval, and an upper well-cemented section which is part of the Ladder interval and is composed of planar cross-sets (Figure 9a).

The Gleann Beag interval at the Moray Firth outcrop is approximately 0.9 m thick. A sub-horizontal compound-set bounding-surface with an observed length of 7 m forms the upper boundary of this unit (Figure 9a). The lower bounding surface cannot be seen. The lower part of the cliff comprises a compound cross-set containing a series of sub-sets that are bounded by inclined subset bounding surfaces. Three sub-sets containing trough cross-laminations are identified with the troughs apparently dipping toward the north-east. The lowermost set on east side (left) is truncated by a second set toward the west, followed by a third youngest set that truncates that cross-set. This kind of sequential lateral truncation and scalloped coset boundary is referred to as "scalloped

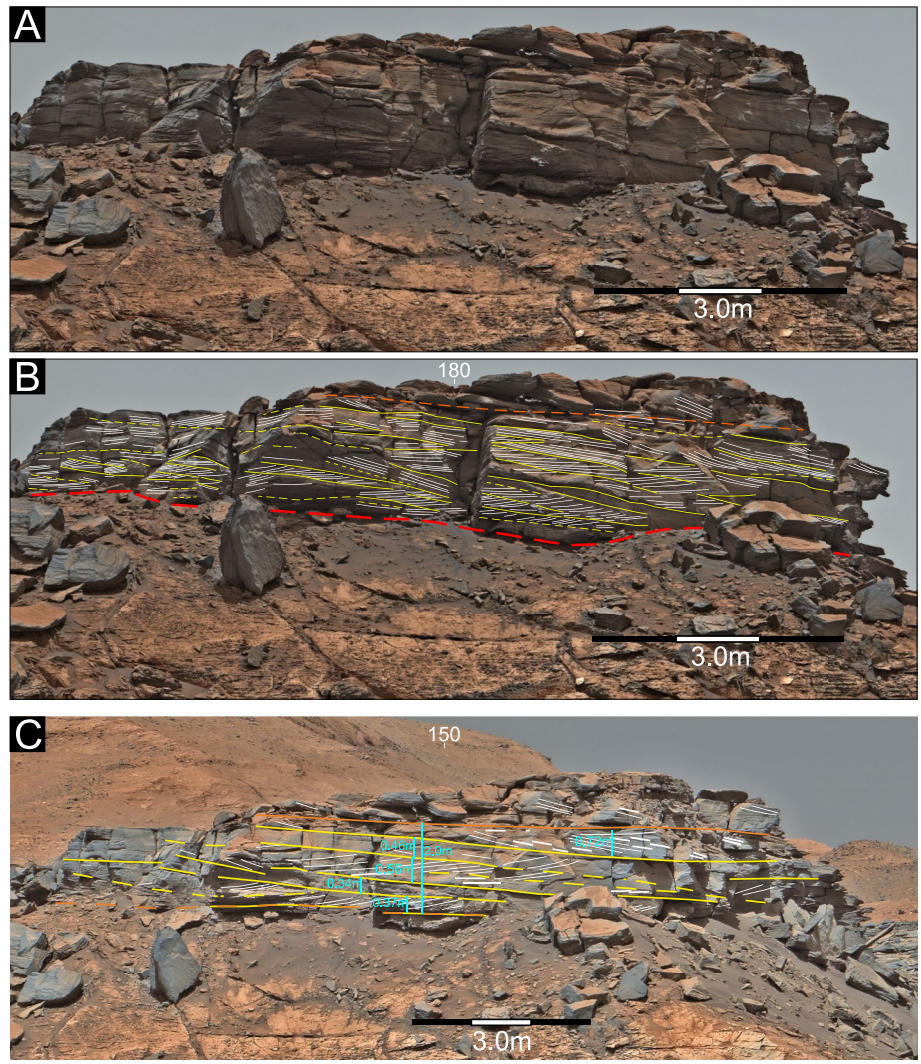

Figure 7. Tower butte outcrop, which illustrates the three-dimensional geometric relationships between cross-laminations, subset bounding-surfaces, and compound-set bounding-surfaces. (a) Uninterpreted view of the north-facing side of Tower butte (b) Interpreted image of the butte, detailing the geometric arrangement of bounding surfaces. Subset bounding surfaces (yellow) typically have an apparent dip toward the west (right of image). The compound-set bounding-surface at the top of the outcrop is sub-horizontal. A detailed interpretation of image 7B (M100 Mastcam mosaic MR_mcam014078, acquired on Sol 2751, at Sol 2747 end-of-drive location). (c) Interpreted mosaic taken from Central butte. From this elevated vantage point, horizontal compound-set bounding-surfaces (orange) can be more readily distinguished from inclined subset bounding surfaces (yellow). A detailed interpretation of image C (M100 Mastcam mosaic MR_mcam13757, acquired on Sol 2618, at Sol 2616 end-of-drive location). The west-facing side of Tower butte is documented in Figure 5a, and contains cross-laminations that are apparently dipping toward the North (left of image). Image credit: NASA/JPL-Caltech/MSSS.

cross-bedding" (Rubin & Hunter, 1983). Cross-laminations within these sets dip north-northeast (average of 16° toward 018°), while their subset bounding surfaces dip toward the northwest (17° toward 310°). The basal coset is also characterized by the presence of pervasive, uniformly distributed nodules throughout the three cross-sets, and throughout cross-sets observed further toward the east (left of the image). These nodules are restricted to the part of the Gleann Beag interval, with an abrupt absence of nodules above the compound-set bounding-surface defining the top of the interval.

Interpretation: This interval is composed of compound cross-bedding, which is readily observed at Tower butte and Moray Firth outcrops. At Tower butte and Moray Firth, subset bounding surfaces and interdune surface are distinguishable. In the ascent area, inclined subset bounding surfaces are identified, however interdune surfaces are not easily recognized.

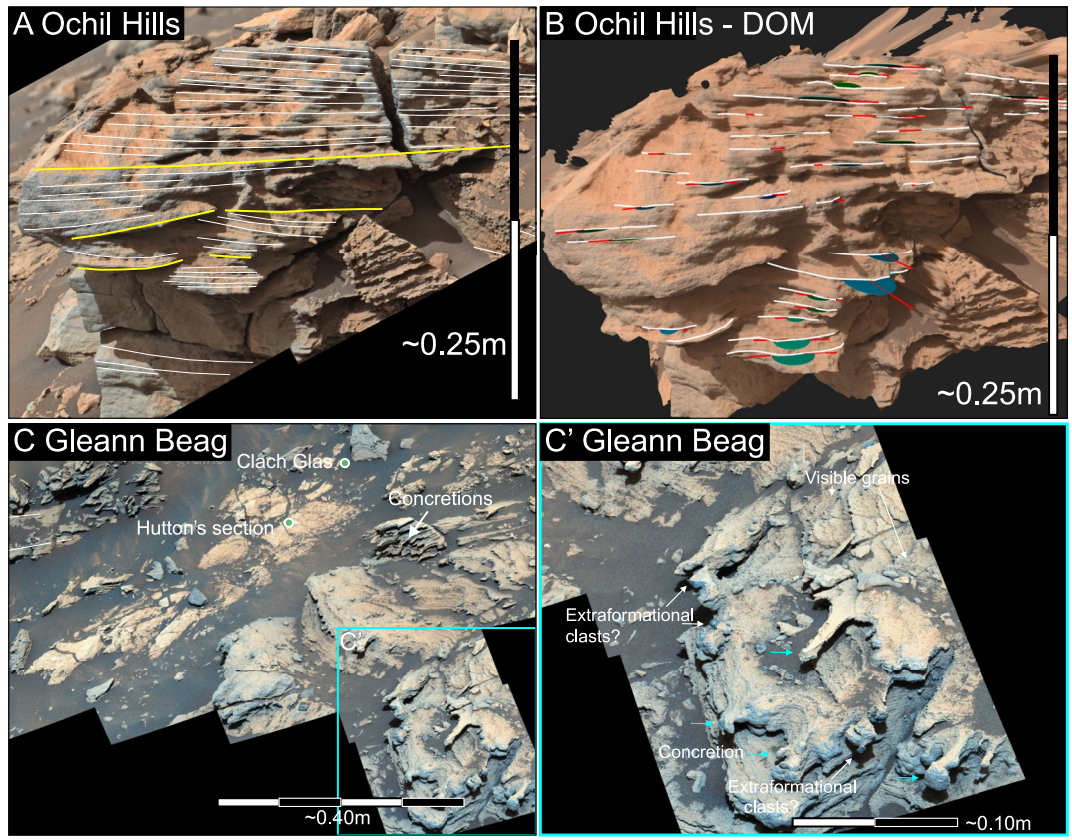

Figure 8. Outcrops within the Glenn Beag interval, immediately above the basal unconformity. (a) Ochil Hills outcrop, composed of cross-bedded sandstones. Dip azimuth of the cross-laminations are broadly toward the Northeast. (M100 Mastcam mosaic MR_mcam14093, acquired on Sol 2694) (b) Digital outcrop model of Ochil Hills, used to measure the dip azimuth of the cross-laminations to determine transport direction. Vector mean of dip-azimuths is toward 061° ($n = 46$). (c) Gleann Beag Mastcam mosaic recording the base of the Gleann Beag interval. Hutton section is interpreted to be part of the underlying (c)Shoemaker formation (M100 Mastcam mosaic MR_mcam14097, acquired on Sol 2695). For mosaic context, see Figure 4a. (c') Close up image of Gleann Beag. Image depicts angular and well-rounded extra-formational clasts derived from elsewhere. Visible grains (that are white) are extra-formational clasts interpreted to be derived from the (c) Shoemaker formation. The lower part of the Stimson also contains sandstone concretions, which formed in situ. Image credit: NASA/JPL-Caltech/MSSS.

At Tower butte, the presence of cross-laminations that dip at a divergent azimuth from their associated underlying subset bounding surfaces are interpreted to be compound cross-sets deposited by oblique compound dunes. Cross-laminations which form the cross-sets, were created by wind-ripple migration and record deposition on the lee slopes of superimposed dunes. The dip-azimuth of the cross-laminations are largely oblique to the dip of the subset bounding surfaces, which indicates the superimposed dunes migrated obliquely across the lee face of the primary dune. The subset bounding surfaces formed by scouring by troughs in front of the advancing superimposed dunes, and they are time-translatent surfaces. These surfaces recorded both the migration of superimposed dunes as they traveled across the lee face of primary dunes, and the forward motion of the primary dunes themself. The orientation of these scour surfaces is dependent on the rate at which both dunes migrate (Rubin, 1987). As a primary dune migrated, it too scoured a sub-horizontal surface–a compound-set bounding-surface–which defined the base of a compound set.

In the ascent area (Figure 4a), dip-azimuths of cross-laminations suggest sediment transport was toward the northeast. The strike of the bounding surface at Enard Bay separating the two troughs gives an indication of the orientation of the trough axis–toward the northeast, suggesting a transport direction to the northeast. The orientation of the cross-laminations and trough axis suggest that the cross-sets here are related by the same transport processes and direction to those observed at Tower butte.

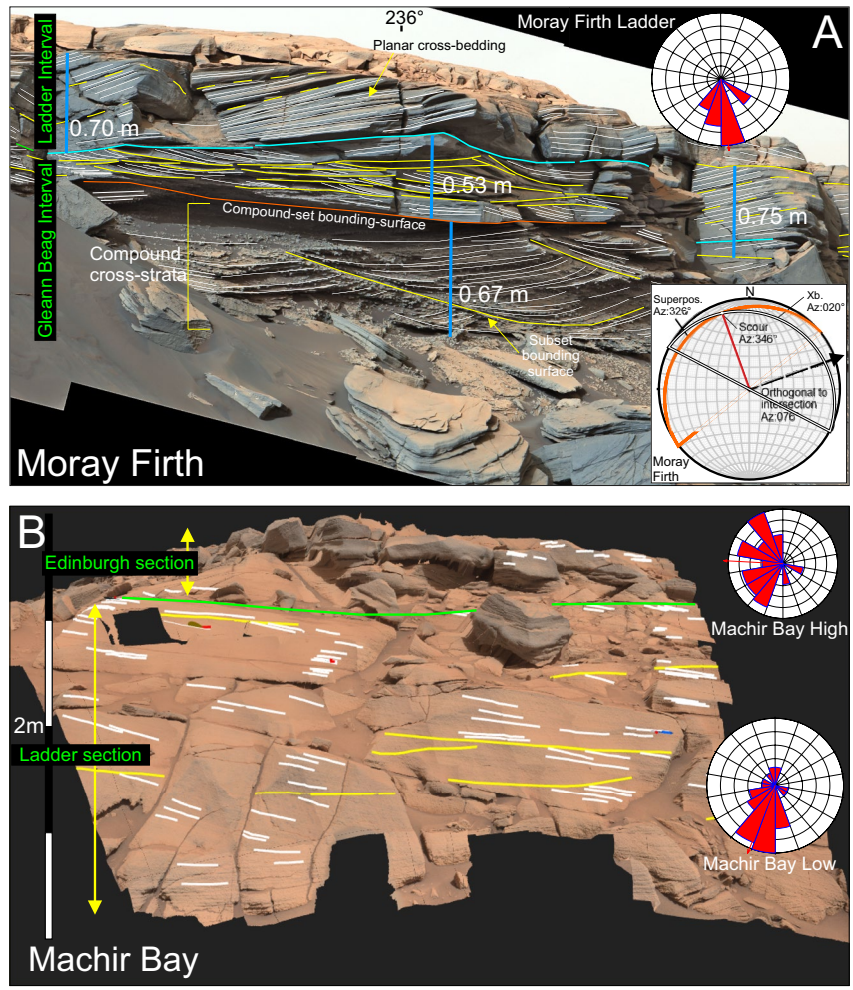

Figure 9. The lower and upper boundaries of Ladder interval. (a) Moray Firth outcrop, which exposes the boundary between the Gleann Beag interval and the Ladder interval. A detailed interpretation of image (a) The cyan line demarks the boundary of the two intervals: the Gleann Beag interval is characterized by compound cross-sets, containing subset surfaces that dip toward the north west, and cross-laminations that dip toward the north east. The overlying Ladder interval contains planar cross-sets that dip toward the south. A detailed photogeologic interpretation of 9a is available here. (M100 mosaic MR_mcam14053, acquired on Sol 2685, at Sol 2664 end-of-drive location). (b) Digital outcrop model of the Machir Bay outcrop, which exposes part of the upper boundary between the Ladder and the Edinburgh sections. Measurement of cross-lamination dip-azimuths, which indicate sediment transport direction were used to delineate the boundary between the two units. An interpreted mosaic of the Machir bay outcrop is available here. An interpreted context mosaic of the Morray firth and Ogre Hill outcrop is available here. Image credit: NASA/JPL-Caltech/MSSS/Joanneum Research/VRVis.

The Ochil Hill target contains an abundance of white grains, which are approximately 0.6–1.2 mm in diameter. These white grains are visually similar in size and color to the C.Shoemaker formation clasts observed at the Hutton's section MAHLI target. They are also located at a similar stratigraphic height, just above the basal unconformity. Analysis of ChemCam targets immediately above the unconformity by Bedford et al. (2022) suggests a hybrid geochemical signature–or mixing–of the local C.Shoemaker formation bedrock, and the capping unit observed higher up in the stratigraphy. This suggests that there could be some amount of sediment erosion and entrainment from the underlying C.Shoemaker formation, leading to this hybrid chemical signature. Similar entrainment of underlying Murray formation clasts has been observed at the Missoula target, at Marias Pass, on the Emerson plateau (Banham et al., 2018).

At the top of the Gleann Beag interval, at the Moray Firth outcrop (Figure 9a), scalloped cross-bedding observed in the lower part of this outcrop can be produced by either fluctuating flow causing a dune trough to scour and fill or by superimposed bedforms migrating along a dune trough (Rubin & Carter, 2006; Rubin & Hunter, 1983). The

latter can be identified by cross-bed dip azimuths that define an asymmetric curve of the subset bounding surface as illustrated in Figure 9a. Because the structure requires both across-crest transport to make the main dune migrate and along-trough transport to cause the scour pits to migrate laterally, it is an indicator of oblique dunes. The divergent orientation of the cross-laminations and subset bounding surfaces suggest that the superimposed bedforms were migrating toward the north-east, while superposition surface is oriented toward northwest. Using the dip and dip azimuth measurements from the DOM, and methods for reconstructing compound bedforms by Rubin and Hunter (1983), the trend of the scour trough was calculated as 346°, which would suggest the superimposed dunes migrated toward 076°–toward the northeast. This lower section is correlated with the Gleann Beag interval observed in the ascent area.

The upper-most portion of the outcrop is interpreted to be composed of a tabular cross-set, belonging to the Ladder interval.

6.2. Ladder Interval: Simple Planar (Straight-Crested) Dunes

The second interval–forming the central unit within the pediment-capping unit–is composed of simple and concordant cross-bedding. Ladder interval outcrops are exposed best near the top of the pediment in west of the study area, near the top of the Moray Firth outcrop and at the Ladder section, but exposures were also identified on the eastern side, at the top of the ascent route at the Machir Bay outcrop. Correlation of this interval is based on foreset dip-azimuths, elevation, and visually tracing of the interval boundaries.

General Description: The base of the Ladder interval is clearly visible at the Moray Firth outcrop at 2/3 of the height of the cliff (Figure 9a – cyan line), and can be traced eastwards toward the ascent area (Figure 6a). The base of this interval is largely planar, undulating little over the width of its exposure: there are no visible scours or sharp-sided palaeotopography. The cross-sets forming this interval are well-cemented and proud-weathering (Figure 9a – above the compound-set bounding-surface). From the side of the capping unit (Figures 4a and 9a) the interval has an apparent thickness of ∼1 m, comprising where a single planar cross-set which forms the edge of the Ladder outcrop (See Figure 4c) can be observed. When observed from the base of the pediment, this cross-set is 0.7 m thick and dips toward the south with a dip-azimuth of 174°. Two subset bounding surfaces can be identified which are concordant with the adjacent cross-laminations. The protruding section of the outcrop (Figure 9a – labeled "Planar cross-bedding") can be observed from the top of the pediment, at the drill site location (Figures 4c and 10a, labeled "Moray Firth").

The Ladder interval is exposed in topographic lows across the upper eroded surface of the pediment capping unit and covers an area greater than 2,500 m^2. In these lows, planar cross-laminations can be seen with an east-west strike and a southward dip-azimuth. These cross-laminations can be traced for distance of over 70 m parallel to strike (Figure 10b), with no major deviations in dip direction observed along a 35 m section parallel to dip. Cross-laminations here appear to be straight, with little or no curvature discerned along their length. Measurement from the digital outcrop model indicates that the average strike of the laminations are toward 112°, indicating that the average dip azimuth is 202°. The top of the Ladder interval–defined by the base Edinburgh interval surface–is best observed at the northern Ladder section and Ladder section, west of the Sol 2702 end-of-drive location (Figures 4c and 10a).

The Ladder interval can be traced east from the Ladder section to the "Sand Pit" area (under the "SW ridge"), and across to the Machir Bay outcrop (Figure 4c). A DOM was used to constrain the dip-azimuth, which was consistently toward the south–toward 200°–across the whole of this interval. Here, the cross-laminations exhibit the same straight, uncurving planform profile and share the same south-dipping trend. These straight, south-dipping laminations can be traced across the Sand Pit to the ridge where the Machir Bay (Figures 6a–6c and 7b) outcrop is located, by the pediment ascent route. South of the Sol 2702 end-of-drive location, in the Sand Pit area (Figure 6c), curved cross-laminations were identified in the otherwise planar cross-laminations of the Ladder interval. The curved laminations are partially covered in sand and occupy an area approximately 8 m across. The strike of these cross-laminations curve from an east-west direction round to a more southerly direction, and laminations have a measured length of approximately 9 m. Surrounding this feature, cross-laminations typically exhibit a southerly dip-azimuth, with an east-west strike, like the rest of the Ladder outcrop.

At the Machir Bay outcrop (Figures 4a–4c and 9b), the base of the Edinburgh interval is identified by a distinct change in the cross-set dip-azimuths between the upper and lower section of the outcrop (Figure 9b). In the lower part of the outcrop, cross-set dip azimuths were focused toward the south (see Figure 9b rose diagram "Machir

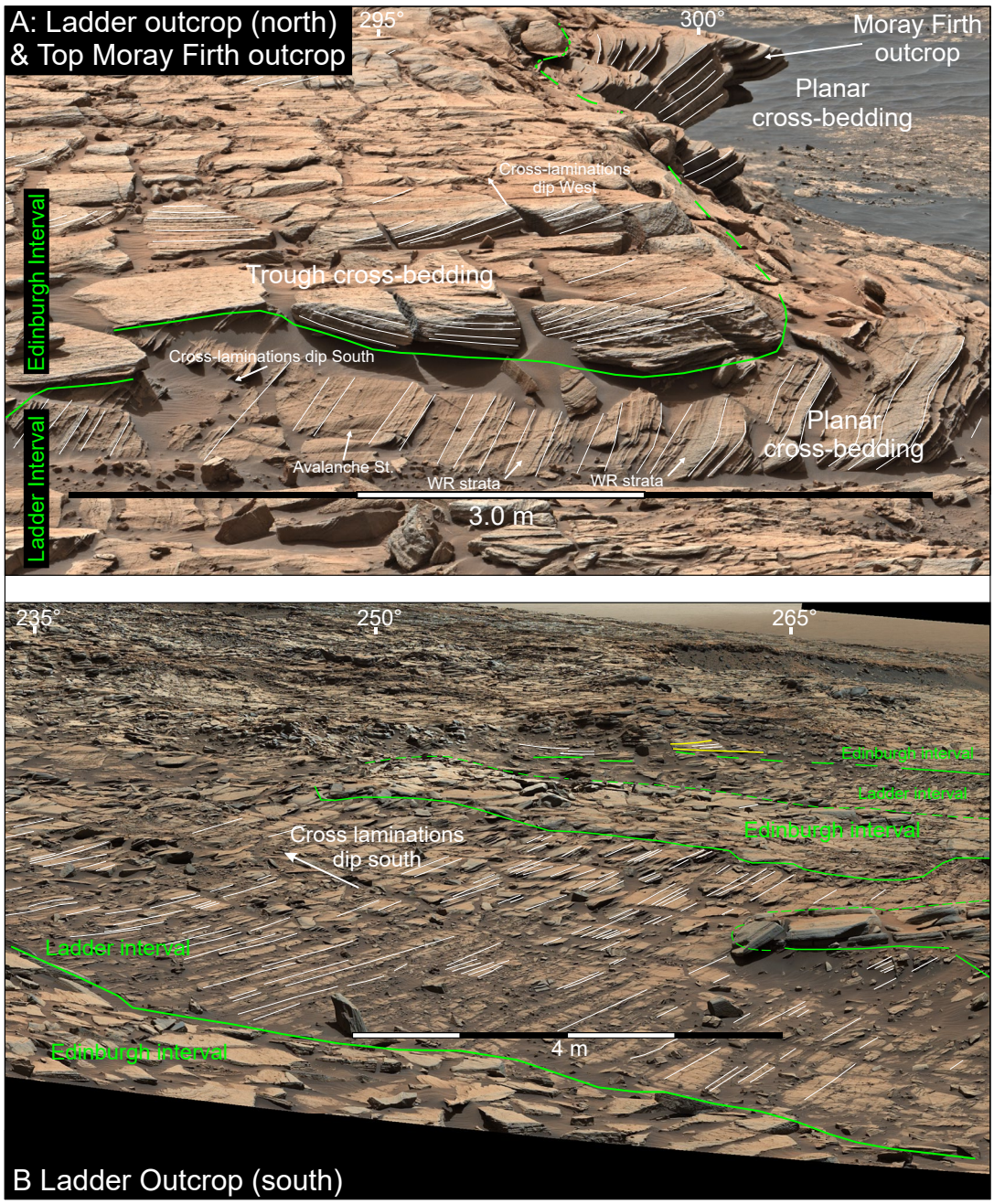

Figure 10. The pediment top, which the Ladder and Edinburgh intervals are exposed. (a) The Ladder outcrop, and the boundary between the Ladder and Edinburgh intervals (green lines). The Ladder interval is characterized by planar cross-bedding, composed of south-dipping cross-laminations. The Edinburgh interval is characterized by trough cross-bedding containing cross-laminations that dip toward the west. See Figure 4c for context, and this associated high-resolution image of Figure 10b. Note relationship of Moray Firth outcrop with Ladder section. (M100 Mastcam mosaic MR_mcam14303, acquired on Sol 2729, at Sol 2702 end-of-drive location). (b) Mosaic showing broader relationship of the Ladder and Edinburgh intervals. The Ladder interval can be traced laterally across the outcrop for distances in excess of 30 m in this image (MR_mcam14220, acquired on Sol 2717, at the Sol 2702 end-of-drive location). Image credit: NASA/JPL-Caltech/MSSS.

Bay low"). In the upper section of the outcrop, a westward bimodal distribution of dip azimuths was identified, which is characteristic of trough cross-sets of the Edinburgh section.

6.2.1. Evidence for Seasonal Wind Variations in the Ladder Interval

Description: At the Ladder outcrop (Figures 10a, 6c and 6c'), cross-laminations dip toward the south, with an average wind-ripple dip-azimuths toward 200°. In the center of the section, a slight change of dip-azimuths direction – approximately 7° – can be observed, which are separated by a subset bounding surface. At an outcrop-scale, cross-laminations appear straight and exhibit no apparent curvature. Close inspection of the strata (Figure 6c) indicates the presence of three distinct types of depositional package, composed of two facies types: avalanche strata, wind-ripple strata, and mixed wind-ripple and avalanche strata (cf. Figure 6c). Twenty-six of these different depositional packages were recorded. Wind-ripple strata formed eight of these packages, with an average thickness of 13.4 cm. Avalanche strata formed seven of these packages, with an average thickness of 14.4 cm. Finally, eight packages of mixed wind-ripple and avalanche strata were identified. These had an average thickness of 30 cm; however, the average thickness was skewed by two packages, measuring 69 and 33 cm respectively. Markov chain analysis was conducted to determine preferential facies transitions. In a down dip direction (north to south), the most common facies succession was wind-ripple strata then avalanche strata, then mixed wind-ripple and avalanche strata before returning to wind-ripple strata. Wind-ripples transitioned to avalanche strata 87% of the time, followed by avalanche strata to mixed strata 62.5% of the time and then back to wind-ripple strata 57% of the time.

Interval Interpretation: The Ladder interval records southward-migrating, simple planar dunes, which marks a major change in dune morphology and sediment transport compared to that of the underlying Gleann Beag interval. The straight, uncurving in planform cross-laminations which are characteristic of this interval indicate that this interval was deposited by straight-crested simple dunes. Foreset dip-azimuth measured across both parts of the outcrop indicate that the sediment transport direction in this interval was toward the south, roughly toward 200°: almost the opposite direction to outcrops associated with the Gleann Beag interval, and much of the rest of the Stimson formation.

Markov chain analysis of the facies packages indicates a common facies sequence: avalanche-dominated strata are typically succeeded by mixed avalanche and wind-ripple facies, which is succeeded by wind-ripple facies. Generally, there is an abrupt transition from wind-ripple strata back to avalanche strata.

Mixed wind-ripple strata and avalanche strata (Figures 5c and 10a) observed in the Ladder outcrop can be used to decipher transport processes on the dune lee slope, and changes to the dominant wind direction which brought about these changes. Sediment avalanching is the dominant transport process where the wind direction is within a few tens of degrees of normal to the dune crest (Eastwood et al., 2012). When the wind direction becomes oblique to the dune crest, wind ripples form and migrate across the dune lee slope. Wind ripple strata commonly forms and accumulates on lee slopes with an incidence angle between 25 and 70°. Incidence angles of less than 27° usually favor bypass and erosion of sediment on the lees surface (Eastwood et al., 2012). Interstratification of the three depositional packages–avalanche strata, wind-ripple strata, and a mixture of the two can be used to indicate changing wind directions. Research conducted by Eastwood et al. (2012) indicates that wind-ripple dominated strata will accumulate between 27 and 45°, mixed strata will form between 27 and 60°, and avalanche dominated strata will form above 60° incidence. Given that the facies change quickly over a short down dip direction, it can be inferred that the wind direction fluctuated over a short episode of time to bring about these rapid facies changes. The absence of internal bounding surfaces could indicate that the set represents a single simple cross-set, or that there are concordant subset bounding surfaces that correspond to flow reversal.

Thus the observed sequence of depositional packages in interpreted to indicate a gradual seasonal transition from wind flow normal to the dune crest, with increasing obliquity of the wind flow direction to the dune crest over a season. Finally, there is an abrupt transition from oblique back to crest-normal wind and sediment transport. The preferential succession of these packages is interpreted to represent a series of annual cycles, where each facies transition is associated with a seasonal changes of wind direction (Hunter & Rubin, 1983; Kocurek et al., 2007). The dunes attempt to align normal to the dominant wind, but will take an alignment that maximizes gross bedform-normal transport to both seasonal winds (Rubin & Hunter, 1987). Assuming that the dominant seasonal wind is much stronger than the others, the dunes may align broadly normal to those winds occur-

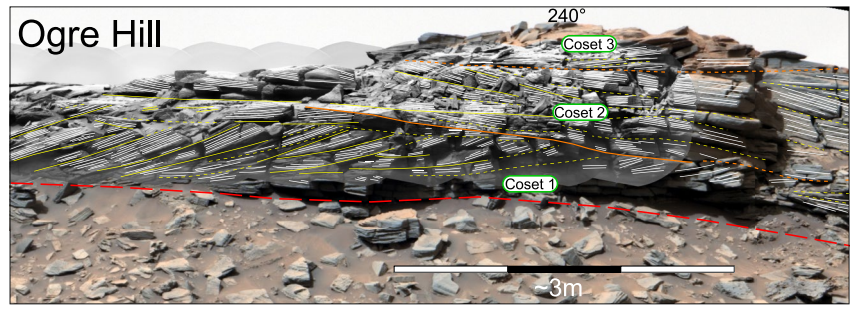

Figure 11. Ogre Hill composite mosaic. Apparent dip-azimuth of coset one is toward the south, which suggests that the lower Gleann Beag interval is absent from this outcrop. Overlying coset 2, and 3 record reversals of dip azimuth, suggesting further flow reversals. Interpreted high-resolution image of Figure 11. (Composite image: MR_mcam14367, acquired on Sol 2741, with ChemCam RMI CCAM04740, at Sol 2734 end-of-drive location). Image credit: NASA/JPL-Caltech.

ring during that one season–possibly the southern spring equinox (Viúdez-Moreiras et al., 2019) or perihelion (Vicente-Retortillo et al., 2018).

6.3. Edinburgh Interval: Sinuous-Crested Simple Dunes

The Edinburgh interval is the uppermost unit of the Stimson formation observed in the study area (Figures 4c and 10). It is composed of trough cross-bedding with foreset dip-azimuths oriented toward the west. The best location to observe this interval is west of the Edinburgh outcrop, in the ridge trending southwest away from the Sol 2702 end-of-drive location (Figure 4c).

Description: On the west side of the Edinburgh outcrop (Figures 4c and 10a) trough cross-sets that are 0.15–0.2 m thick are visible. The basal surface of these troughs appear to cut down into the underlying cross-sets of the Ladder interval. Trough cross-sets can be observed as far west as the top of the Moray Firth outcrop, where part of the Ladder interval is exposed (Figure 10a – Moray Firth lable). To the east, the Edinburgh interval can be traced as far as the Machir Bay outcrop, where the top cross-set contains westward-dipping sets (Figures 4c and 9b). In some sections, small, isolated concretions can be observed. The area surrounding the Edinburgh drill site is characterized by trough cross-sets exposed in planform, preventing measurement of the cross-set thickness. Where visible, foreset dip-azimuths are oriented west in the area around the drill site. Cross-sets compose the southwest-trending ridge, southwest of the dill site. The ridge is approximately 1.5 m thick, measured from the top of the Ladder outcrop to the top of the ridge and is composed of stacked cross-sets. On the top of the SW trending ridge, cross-sets were observed to dip toward the west (Figures 4c and 10b).

Interpretation: The Edinburgh interval is defined by its westward palaeotransport direction. The interval is characterized by trough cross-bedding which implies that bedforms which generated these strata were sinuous crested, in contrast to the straight-crested dunes which deposited the planar cross-sets in the Ladder interval. Whether these sinuous-crested dunes were simple or superimposed on a larger primary dune is uncertain: no subset bounding surfaces were observed in the Edinburgh interval due to the planform view of the outcrop afforded by the rover.

6.4. Ogre Hill Outcrop: Further Evidence of a Fluctuating Sediment Transport Direction

The Ogre Hill outcrop provides additional insight to changing of sediment transport direction. The outcrop is located 60 m west of the Edinburgh drill site (Figures 1b and 11). Because of the outlying position relative to the rest of the outcrops, and the perceived lateral thinning and pinch-out of the Gleann Beag interval, correlation was considered unreliable.

Description: In this outcrop, cross-laminations and cross-sets were observed in cosets that are between 0.25 and 1 m thick. The outcrop can be sub-divided into three cosets. The lowest package–Coset 1–overlies the base Siccar Point group unconformity. At the base of this outcrop section, the unconformity is uneven and undulates. Coset 1 contains curved subset bounding surfaces (yellow surfaces in Figure 11) that dip toward the south. The cross-laminations within these cross-sets are concordant to their lower subset bounding surfaces. Coset

two overlies the basal coset and is has an undulating basal compound-set bounding-surface. Within the coset, concordant subset bounding surfaces form north-dipping, low-angle, curving, erosional surfaces, which appear to become straighter and more steeply inclined toward the south end of the outcrop (left of the image). Within each of the cross-sets bounded by the subset bounding surfaces, the cross-laminations are near-parallel, dipping at an angle close to that of their underlying bounding surface. Coset 3, at the top of the succession is relatively thin and is poorly resolved. It contains cross-sets and subset surfaces which dip toward the south: the opposite direction to the underlying coset 2. The basal compound-set bounding-surface is horizontal and shows little relief.

Interpretation: Cross-bedding at Ogre Hill is interpreted to record a complicated history of changing sediment transport directions. The apparent reversal of dip direction observed between each coset possibly suggests a major change–or reversal–of wind direction. Although there is no way to directly correlate the Ladder interval and coset 1, both cosets share a similar sedimentary architecture (subset bounding surfaces with concordant cross-laminations) and dip in the same direction. The Gleann Beag interval apparently pinches out west of Moray Firth outcrop, and is not observed at Ogre Hill.

Subset bounding surfaces, with concordant cross-laminations can be interpreted as reactivation surfaces, caused by brief episodes of flow reversal (third order surface – Brookfield, 1977) where the lee slope is degraded, forming a low-angle bounding surface (Hunter & Rubin, 1983). These might be associated with a seasonal change of flow, but no long-term change of transport direction (Kocurek, 1991; Mountney, 2006). To change the dip-azimuth of the cross-laminations, and for them to be preserved as seen in the outcrop, would require a complete reorganisation of the dunes, with the dune reforming with the lee slope on the opposite side of the dune. The dune would then have to migrate at least one dune wavelength to scour a continuous lower bounding surface. Stacked cosets with reversed dip-azimuths would suggest that several generations of dunes migrated across this location. This would suggest a prolonged period of wind reversal (see Section 7).

7. Palaeotransport Analysis

The strata preserved at the Greenheugh pediment records a complex history of bedform migration patterns, which provide an indication of sediment transport directions, and changes in the prevailing wind over time. Several approaches have been taken to document the foreset dip-azimuths of cross-sets in this outcrop: Visual estimation of dip-azimuth; measurement using digital outcrop models; and stereonet reconstruction of compound sets using perpendicular cliff faces. For this section, subtle seasonal changes in sediment transport direction (typically preserved as interbedded avalanche and wind-ripple strata) will be excluded. Focus will be on the larger-scale trends observed within the vertical succession.

7.1. Gleann Beag Interval: Reconstruction of Compound Cross-Sets

Compound cross-sets were observed at Tower butte and Moray Firth outcrops. The geometric relationship between the superposition surfaces (subset bounding surfaces) and the cross-laminations can be used to reconstruct the compound bedforms using techniques described by Rubin and Hunter (1983), and which were implemented by Banham et al. (2021) at the Murray buttes. For these two outcrops, bounding surfaces and cross-laminations were plotted as planes on stereonets to determine the long-axis trend of the scour trough, and the migration vector of the superimposed dunes (Figure 9a insert).

At Tower butte (Figure 7), cross-laminations and subset bounding surfaces dip-azimuths were estimated to be 17° toward 027° for cross-laminations and 12° toward 321° for subset bounding surfaces. The intersection of these planes gives the trend of the scour trough toward 340°, which means the migration direction (which is orthogonal to the scour trough trend) is toward 070°. This suggests that the superimposed dunes were migrating close to perpendicular to the crestline of their host dune.

At Moray Firth outcrop (Figure 9a – Gleann Beag interval), dip-azimuths were derived from a digital outcrop model. The average cross-lamination dip-azimuth was 16° toward 020° ($N = 7$), with the subset bounding surface dip-azimuth measured as 14° toward 236° ($N = 8$). The intersection between these planes indicate a scour trend of 346°, and a superimposed bedform migration direction toward 076°. As with Tower butte, this relation suggests that the superimposed bedforms would have migrated perpendicular to the crestlines of the primary dunes.

7.2. Visual Estimation of Dip-Azimuths

Visual estimation of cross-set dips was performed at various locations across the traverse, specifically in areas where stereo images were not obtained, or beyond the range where digital outcrop model construction is feasible. This method was also used at several other outcrops where digital outcrop models were constructed, to validate the method. In total, dip-azimuth of 33 cross-laminations and four measurements of subset bounding surfaces were made. These data, estimated using methods described by Banham et al. (2018, 2021), were plotted on a HiRISE orthomosaic to show the spatial relationship of the dip-azimuths (See Supporting Information S1). Generally, these measurements reflect the measurements taken using digital outcrop models: Foreset dip-azimuths are typically: northeast in the Gleann Beag interval; southward in the Ladder interval; and no visual measurements were made in the Edinburgh interval. At Ogre Hill, dip-azimuth of the cross-laminations was observed to switch directions–to reverse dip direction (Figure 11)–depending on the coset observed. Because this outcrop is outlying and was not correlated to the main outcrop of the study area, it will not be discussed further in this section.

7.3. Digital Outcrop Models (DOMs)

In total, 574 dip-azimuth measurements were taken across 20 digital surfaces rendered from stereo images. These were used to constrain the palaeotransport directions and aided defining the three key intervals observed. These data were plotted in stereonets, and then displayed spatially with their associated interval on an outcrop model generated using OnSight (Abercrombie et al., 2017): Figure 12 highlights the distinct palaeotransport direction for each interval, and the mapped spatial extent of the stratigraphic intervals. For the data collected using DOMs, the vector mean and vector magnitude of the cross-lamination dip azimuth was calculated using a trigonometric method described by Lindholm (1987). The vector mean and vector magnitudes for each interval respectively are: Gleann Beag, vector 024.9°, magnitude 0.56 ($N = 248$); Ladder, vector 200.8°, magnitude 0.76 ($N = 210$); and Edinburgh vector 278.9°, with a magnitude of 0.66 ($N = 116$).

7.4. Interpretation of Palaeotransport Data

The Gleann Beag interval, which forms the basal portion of the Stimson formation here is composed of cross-bedding with a dip-azimuth trending toward the northeast, suggesting sediment transport toward that direction. In two locations – Tower butte, and Moray Firth outcrop – compound cross-bedding has been identified, recording the migration of oblique compound dunes. These suggest a more complex sediment transport regime, where superimposed bedforms migrated more toward the east-northeast, rather than the north-northeast suggested purely by the cross-lamination dip azimuth.

The Ladder interval, which forms the central unit of the Stimson here is composed of simple planar cross-beds which dip consistently toward the south (vector magnitude of 0.76). The planar cross-sets suggest simple dunes with net sediment transport across the crests from north to south. This does not account for sediment transport oblique to the dune crestlines, as represented by the wind-ripple strata observed at the Edinburgh section outcrop of the Ladder interval.

The Edinburgh interval represents the top-most Stimson unit in the study area. The interval is mainly composed of trough cross-bedded sandstone, with a dip-azimuth vector mean oriented toward the west. Because few bounding surfaces could be identified or mapped, it is uncertain whether these trough cross-sets are associated with sinuous-crested simple dunes, or if they are superimposed dunes on a compound dune. This would have a bearing on the sediment transport direction: westward, if the dunes were simple, or a more northward transport direction if they form part of compound dunes migrating toward the north.

8. Discussion

8.1. Interpretation of Aeolian Surface Processes

The pediment capping unit is predominantly composed of cross-strata containing thin, uniform cross-laminations interpreted to be of aeolian origin. Close inspection of MAHLI images indicate sedimentary textures commonly observed in sandstones transported by wind action: well-rounded grains; a bimodal grain-size distribution, and

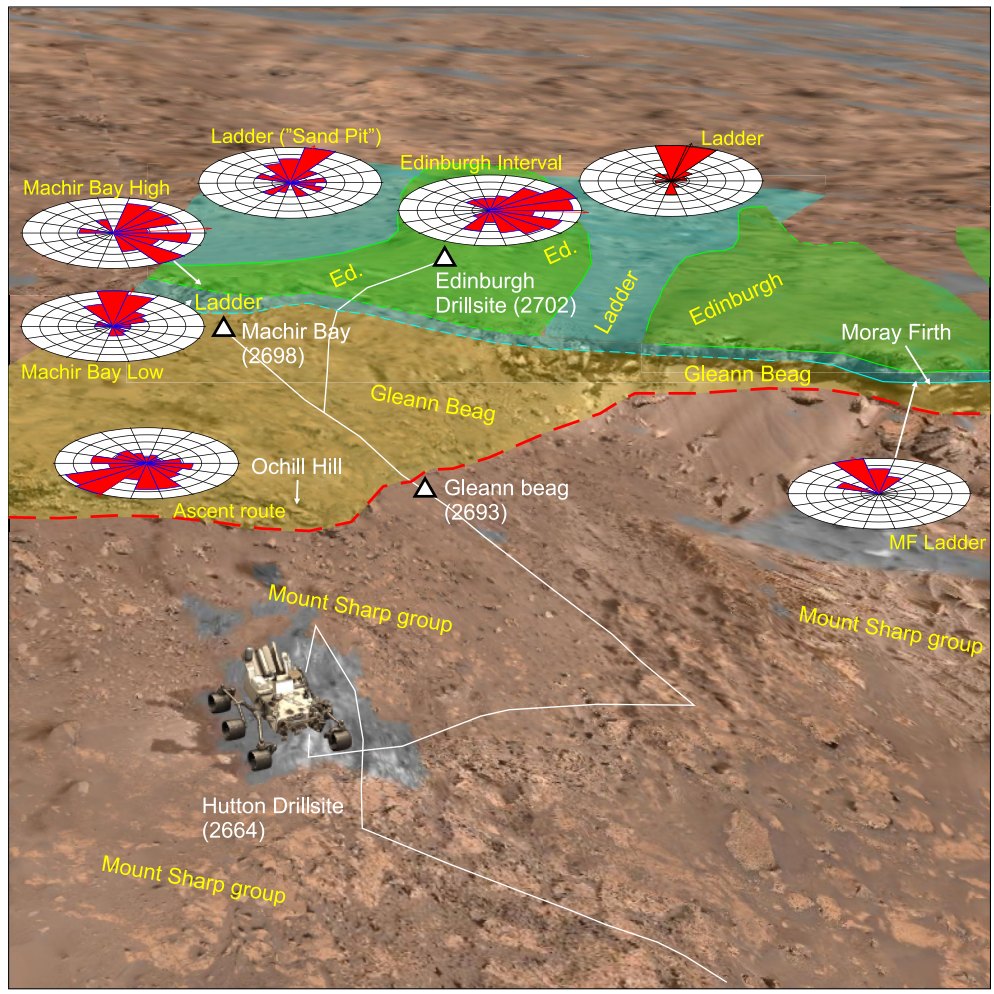

Figure 12. Diagram depicting palaeotransport direction in relation to the different stratigraphic intervals. Rose diagrams show the net sediment transport direction measured at each of the key outcrop locations, in relation to their relevant stratigraphic interval. This image was generated using NASA OnSight software (Abercrombie et al., 2017).

development of wind-ripple laminations associated with that bimodal grain-size distribution. The geometric mean grain size across the Stimson formation observed at the Greenheugh pediment is 486 μm. While the mean geometric grainsize is coarser than that observed at the Emerson plateau (406 μm; Banham et al., 2018), the 80 μm difference in grain size does not preclude aeolian transport processes: larger grains are commonly transported by surface creep, and mean grain sizes up to 660 μm have been observed on dunes in the Libyan desert (Ahlbrandt, 1979). There is, however, an interesting and clear disparity between the gran size of ancient aeolian strata, and modern aeolian dunes in Gale. The average grainsize of the Stimson is between 400 and 450 μm, however studies on modern aeolian sediments in Gale have observed average grainsize of 112 μm (Sullivan & Kok, 2017), 120 μm (Ehlmann et al., 2017), and 113 μm (Ewing et al., 2017). In modern coarse-grained ripples, grains of up to 500 μm are commonly observed near ripple crests, and grains as large as 1,500 μm are identified on ripple stoss slopes (Sullivan et al., 2020; Weitz et al., 2018), which may have been moved by either reptation or surface creep. In terms of rounding, the grains observed at the Greenheugh pediment are well-rounded similar to the grains observed at Williams outcrop on the Emerson plateau (Banham et al., 2018). This degree of rounding results from the high impact velocities associated with aeolian transport (Folk, 1980; Sullivan & Kok, 2017). Grainsize and sorting trends observed across the Stimson formation are apparently similar to grainsize and sorting trends observed on Earth. Sands in upwind areas closer to the source tend to be coarser and more poorly sorted, becoming progressively well sorted toward the erg center (Lancaster, 1995). These trends result from larger, slower moving grains remaining in the upwind areas.

Wind-ripple laminations observed across the study area, and specifically at Enard Bay and Edinburgh targets are diagnostic of aeolian transport processes. Migration of wind-ripples generates inverse-graded laminations, which have are highly uniform in thickness across a laterally persistent distance (Fryberger & Schenk, 1988; Hunter, 1977; Sharp, 1963). The final features diagnostic of aeolian facies are the avalanche strata, seen at the Edinburgh outcrop of the Ladder interval. These laterally discreet, tongue-shape sediment packages form by repeated failure of the dune crestline at multiple locations along the length of the dune (Hunter, 1977). The avalanche deposits are loosely packed, and form interbedded tongues which are visually distinctive, and tend to be wider on sub-aqueous dunes (Hunter, 1985).

8.2. Morphology and Dimensions of Dunes Recorded in the Intervals

Three distinct types of cross-sets can be observed at the Greenheugh pediment, each of which can be linked to three types of dune morphologies. The morphology of the cross-sets is directly related to the migration and interactions of dunes, and surface processes occurring on the dunes. The lowermost Gleann Beag interval is characterized by compound cross-bedding generated by superimposed bedforms migrating across the lee of a dune (Figure 13a) (Rubin & Hunter, 1983); the Ladder interval is characterized by simple planar cross-bedding likely generated by straight-crested simple dunes, and the Edinburgh interval contains trough cross-bedding generated by a sinuous-crested simple-dune.

8.3. Compound Cross-Sets Formed by Oblique Compound Dunes

These compound cross-beds, much like those observed at the Murray buttes (Banham et al., 2021) were deposited by small superimposed dunes migrating across the surface of a larger primary bedform, also commonly known as a compound dune, mega dune, or draa (Figure 13a). As the superimposed dune migrates across the lee of the primary dune, the scour trough preceding the dune scours a superposition surface, which is then overlain by cross-laminations deposited on the lee slope of the superimposed dune. Estimating the size of these dunes is difficult, as the angle of climb is undetermined, and because the divergence between the resultant transport directions has a bearing on bedform height (Rubin & Hunter, 1985). A first-order approximation of the dune height can be made by assuming cross-set and coset thickness are proportional to the dune height. Cosets, representing the preserved lower section of a compound dune, have thicknesses of 2 m at Tower butte. Assuming that the compound dune's original height was one order of magnitude taller than the preserved thickness, it could be reasonable to assume that the compound dunes here were ∼20 m tall. If the same estimate is applied to the cross-sets bounded by subset bounding surfaces, which represent superimposed dunes, their estimated height could be 3–5 m tall. Assuming both types of dune have a bedform index of 15 (Wilson, 1972), compound dunes may have wavelengths of 300 m, where superimposed dunes have wavelengths of 45–75 m. These attributes are comparable to the dunes reconstructed at the Murray buttes (Banham et al., 2021), in part because the cross-set and coset thicknesses are similar.

8.4. Planar Cross-Sets Formed by Reversing Simple Dunes

These planar concordant compound cross-sets are interpreted to represent the migration of a straight-crested simple dune formed in a fluctuating flow (Figure 13b). The straight cross-laminations can be traced for >70 m parallel to their strike, which suggests they were formed by dunes with little or no crestal sinuosity (Rubin & Carter, 2006). It could be possible that the laminations are slightly sinuous at a hectometer scale–formed by a dune with a crestline in excess of half a kilometer–however this scale of observation was not possible with this outcrop. Simple dunes can form in unidirectional winds, however, dunes formed within a reversing flow tend to achieve straighter crestline profiles due to along-crestline coupling (Rubin, 2012). Evidence of along-crest sediment transport which would enhance crestline coherence is provided by intercalation of wind ripples and avalanche strata seen at the Edinburgh section. Avalanche strata typically forms because of crestline-normal sediment transport, where wind transport sediment perpendicular across the crestline onto the lee slope, causing avalanches. Wind ripple strata tend to form where wind transports sediment oblique to the dip of the dune lee slope (Eastwood et al., 2012), which would provide the coupling effect to form a straight-crested dune. Concordant subset bounding surfaces observed in the Ladder interval at the Moray Firth outcrop and the Edinburgh outcrop are interpreted to be reactivation surfaces. These types of erosional surfaces commonly form as a result

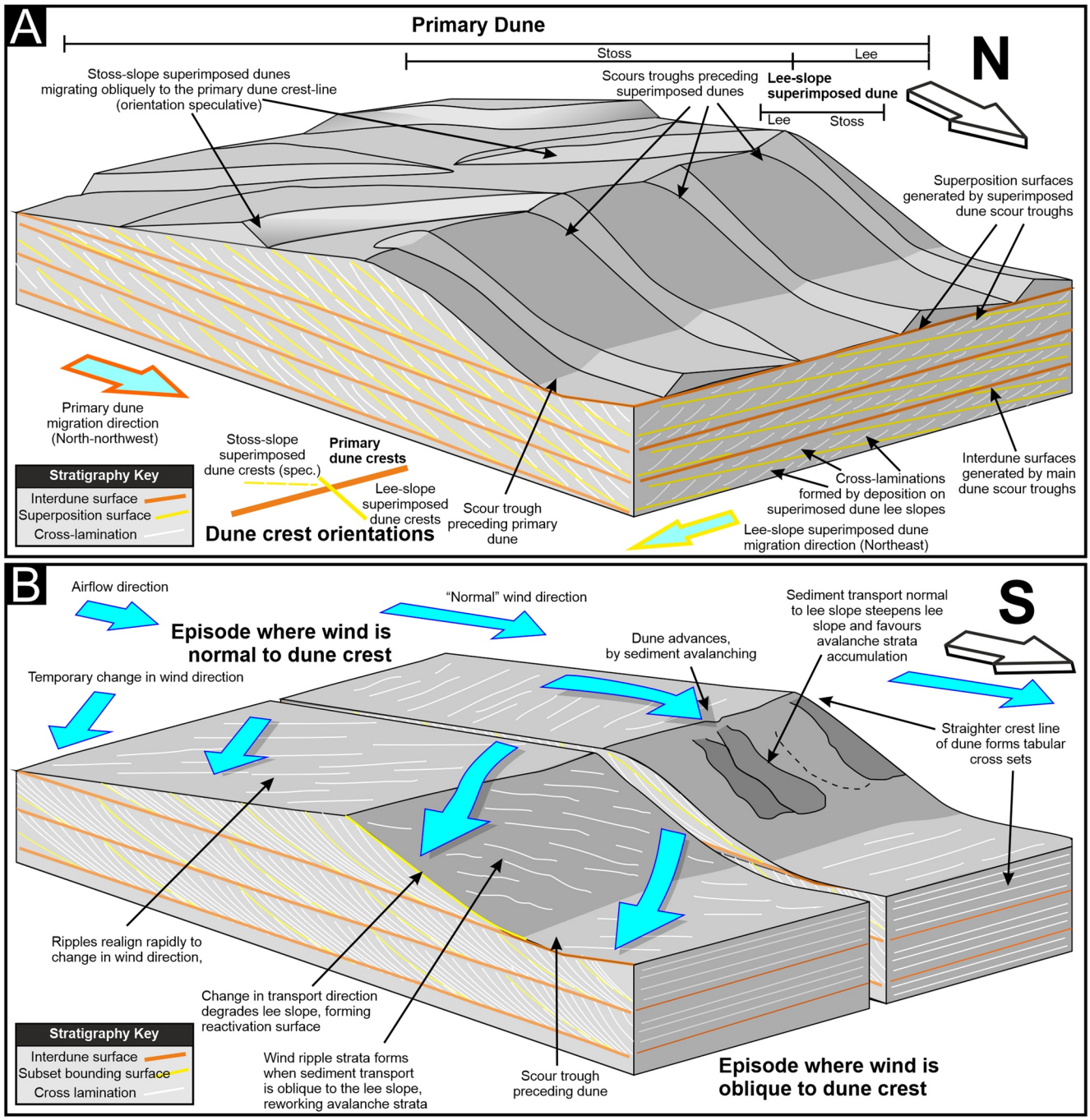

Figure 13. Reconstruction of bedforms interpreted from the Stimson formation exposed the Greenheugh pediment. (a) Schematic representation of compound bedforms interpreted to have deposited the Gleann Beag section. Primary dune lee-slopes are interpreted to dip toward the north or north-north west. Lee-slope superimposed dunes are interpreted to be migrating roughly toward the northeast, while stoss-slope superimposed dunes inferred (see text for details). (b) Schematic representation of bedform responsible for depositing the Ladder section.

of wind reversal, which would provide a further coupling effect (Rubin, 2012). Because these bounding surfaces tend to form parallel or very close to parallel, they can be difficult to identify in planform sections, such as at the Ladder section. Similar concordant subset bounding surfaces can be identified at Ogre Hill, which can also be interpreted as reactivation surfaces caused by fluctuating or reversing flow. Estimating the bedform height, using a similar first-order approximation would suggest the bedforms were approximately 7–10 m tall, with wavelengths of 150 m. It should be noted that on Earth, straight-crested transverse dunes are relatively rare, and

that straight-crested dunes are typically either linear dunes or barchan dunes in the "fingering-mode" (sensu Courrech du Pont et al., 2014). Another consideration is that complex dune interactions can result in apparent deflection or reversal of sediment transport locally at the dune scale or even on different parts of the dune (Brothers et al., 2017; Pedersen et al., 2015). These types of interaction could result in an apparent reversal or deflection of sediment transport as seen in the Ladder interval.

8.5. Trough Cross-Bedding of the Edinburgh Interval

Trough cross-beds are observed to form the bulk of the Edinburgh interval. As this interval was mostly viewed in planform, it was not possible to identify subset bounding surfaces indicative of compound dune migration. Two valid interpretations for this interval are possible: the trough cross-sets could form parts of sinuous-crested simple dunes that migrated toward the west; or trough cross-sets could form part of compound cross-sets formed by dunes migrating obliquely across a primary dune's lee slope. No subset bounding surfaces were identified in the planform section of the Edinburgh interval, reducing confidence in the latter interpretation. If the cross-sets represent migration of sinuous crested dunes, this would suggest that the wind direction was uniformly toward the west, with little flow reversal, or oblique sediment transport which could provide any coupling effect to straighten the crestline (Rubin, 2012). Regardless of the type of dune that generated the Edinburgh interval, the westward sediment transport direction contrasts with the southerly transport direction of the underlying Ladder section.

8.6. Dune Migration: Direction, Duration, and Preservation

The dip-azimuth and the number of stacked, preserved cross-sets encode information relating to the wind directions, long-term sediment transport direction, and preservation or deflation of strata. Changes in wind direction are preserved across multiple temporal scales: from seasonal wind variations to longer term ~millennial time frames.

The Gleann Beag interval is characterized by compound cross-sets deposited by the migration of oblique compound dunes. The geometric relationship between the cross-lamination and superposition surface dip-azimuths provide insight into the relative migration directions of the dunes (Almeida et al., 2016; Rubin & Hunter, 1983). Based on observations at Tower butte and Moray Firth outcrop, the superimposed dunes migrated generally toward the northeast, while the compound dunes migrated toward the north, or north-northwest, as observed at the Murray buttes. These oblique compound dunes require a bimodal or multi-modal wind regime to form, where the two dominant wind directions are obtuse (Courrech du Pont, 2015; Derickson et al., 2008; Havholm & Kocurek, 1988; Rubin & Hunter, 1987).

Sediment transport for the Gleann Beag interval matches the net sediment transport direction for the Murray buttes and Emerson plateau (Banham et al., 2018, 2021). This similar transport direction also supports geochemical evidence which suggests that the sedimentary provenance of the Gleann Beag interval is the same as that at the Emerson and Naukluft plateaus (Bedford et al., 2022; Thompson et al., 2022). This interval, and the rest of the Stimson formation represent a relatively stable and prolonged period of net sediment transport toward the north, or northeast. The Stimson formation at the Murray buttes has a recorded thickness of >15 m (Banham et al., 2021), and the Gleann Beag interval has a recorded thickness of 3.6 m. Assuming that the strata at the Murray buttes and Gleann Beag interval are contemporaneous, or at least penecontemporaneous, these strata will represent a minimum of several thousand years of sediment accumulation, based on typical dune migration rates from Earth or Mars (Boazman et al., 2021; Chojnacki et al., 2019; Davis et al., 2020; Phillips et al., 2019). However, beyond this observation of common depositional architecture, geochemistry, and sediment transport direction, there is no evidence that the strata at these two locations are time-equivalent.

The Ladder interval contains a south-dipping cross-set and overlies the Gleann Beag interval. It is composed of strata deposited by southward transported sediment. For the Ladder interval to accumulate, sediment transport was reversed for a prolonged period: long enough for the dunes to reform with the lee slope oriented toward the south, and then for dunes to migrate at least 1–2 two wavelengths to deposit and preserve a single south dipping cross-set. An estimate of migration rate can be made from the inter stratified lee-slope deposits observed at the Edinburgh section. Assuming that a single seasonal cycle is represented by the facies transition from wind-ripple to avalanche to mixed strata, a migration rate of 0.3–0.5 m per annual cycle can be assumed, (which is comparable to modern migration rates on Mars of 0.3 m/EY and 0.2–1.1 m/EY (Boazman et al., 2021; Davis et al., 2020))

and that the planar cross-set was formed by a dune with a 150 m wavelength, net sediment transport would need to be toward the south for at least 300–500 Mars years to form the cross-set. Sediment transport toward the south may have persisted for longer, however, evidence of overlying cross-sets was removed by aeolian deflation and were lost from the stratigraphic record before deposition of the Edinburgh interval.

At shorter time scales, the intercalated aeolian strata at the Edinburgh section are interpreted to represent seasonal changes in wind direction, and episodic wind reversals. Avalanche strata typically form when sediment is transported normal to the crest line, whereas wind-ripple strata forms during times when wind is oblique to the crestline (Eastwood et al., 2012). The predictable facies succession observed at the Edinburgh section is interpreted to arise because of seasonal changes in wind direction, where bedform-normal transport occurs during a period of stronger winds (typically spring on Earth), and subsequent wind-ripple strata form during other parts of the year when the seasonal wind is oblique to the crestline. These seasonal (and even diurnal) trends are common on Earth, both in the modern environment (Ewing et al., 2006; Havholm & Kocurek, 1988; Hunter & Richmond, 1988) and in the stratigraphic record (Chan et al., 2000; Uličný, 2004). Episodic flow reversal is also recorded in the Edinburgh section. Dunes formed in reversing flows typically have straighter crestlines (Rubin, 2012), which in this case, is preserved as the extremely straight cross-laminations of the Edinburgh section. Reactivation surfaces are also identified in the Edinburgh section. These can arise from deflation and degradation of the lee slope by: reversal of airflow; changes in dune size, shape, crestline-sinuosity or migration direction; or as a result of dune interactions. Reactivation surfaces formed by flow reversal would have dip-azimuths parallel to the cross-laminations and would be difficult to identify. One reactivation surface was identified at the Edinburgh section, which had an angular discordance, indicating that it may record a change in dune size, shape, or migration direction.

Finally, the Edinburgh interval potentially records a more unimodal sediment transport direction toward the west. Trough cross-bedding arises from the non-uniform advance of the dune lee slope, forming sinuous-crested dunes. Here, flow reversal or crestline coupling by oblique airflow would cause crestline straightening, and planar cross-sets to form.

8.7. Stratigraphic Architecture

The boundaries between each of the intervals–where a major change in the sediment transport direction is recorded could represent major gaps in the stratigraphic record at the Greenheugh pediment. With minimal loss of strata, the base Ladder interval bounding surface may represent near continuous sediment accumulation: transport direction reversed rapidly with little or no sediment bypass, and the lee slope and scour trough reformed immediately on the south side as the dune migrated south. Conversely, the base Ladder interval bounding surface could also represent a prolonged period of sediment bypass or deflation: an aeolian supersurface (Blakey, 1988; Havholm & Kocurek, 1994). This would represent an intraformational unconformity, where some amount of strata may have accumulated, was then scoured, and was lost from the stratigraphic record. Such surfaces are documented to form when unconsolidated sand is deflated, scouring the accumulated strata down to the water table, where cohesion prevents further erosion (Cardenas et al., 2019; Fryberger et al., 1988; Kocurek & Day, 2017; Mountney, 2006; Mountney & Russell, 2009; Mountney & Thompson, 2002). However, within the Stimson formation, micro-topography or other structures which would indicate a damp depositional surface have not been identified on or near these interval boundaries.

A major allogenic change that would form a supersurface or cause prolonged reversals of sediment transport would affect the whole dune field and would be expressed across the preserved stratigraphic accumulation. The Greenheugh area being the only part of the Stimson succession which preserves this southward sediment transport suggests that it is higher in the stratigraphy than preserved at the northern Stimson outcrops. This sediment transport reversal would have occurred across the dune field, but it has been eroded from the top of the succession preserved in the northern outcrop areas. Corollary questions are whether the compound cross-sets at Murray buttes and at Tower butte are contemporaneous, and how much strata are missing between the two preserved sections of strata? That both outcrops are the preserved expression of oblique compound dunes, migrating in a near identical direction could suggest that they are genetically and temporally linked, and that the northern Stimson outcrops form a broader, lower part of the Gleann Beag interval.

There is a possibility that the Ladder interval simply represents autogenically–controlled changes in dune migration direction, for example, where interacting dunes result in a local reversal of sediment transport (Ewing & Kocurek, 2010), or where a slight change of transport ratios results in a reorganization of the dune (Rubin, 2012). These interactions would occur across a small spatial extent in a dune field and would be preserved in a yet smaller volume of strata. The observed Ladder section covers an area of >400 m^2 (>1 km^2 if the Ogre Hill outcrop represents part of the Ladder interval). Correlation of the Ladder interval across this extent (e.g., to the east side of the pediment), would favor the interpretation of allogenic controls on sediment accumulation.

9. Conclusions

1. The Greenheugh pediment capping unit is formed of a dark-gray erosion-resistant sandstone. Textural analysis of grains across the pediment confirm that the sandstone is composed of well-rounded sand grains, with a bimodal grain-size distribution, and that in some locations, inverse grading of grains within wind-ripple laminations can be seen. These observations are consistent with aeolian transport processes.
2. The Greenheugh pediment capping unit is interpreted to be a continuation of the northern Stimson formation outcrops (Emerson, Naukluft, and Murray buttes). All outcrops share a common depositional architecture and sedimentary facies, which indicate that they were deposited by the same processes. All outcrops overlie the base Siccar Point group unconformity. However, it is uncertain whether the Greenheugh Stimson outcrops are time-equivalent to the northern Stimson outcrops: there is no way to correlate the outcrops with any degree of certainty, but geochemical analysis (Bedford et al., 2022) provide some indication that the Gleann Beag interval is correlative to the Stimson at the Emerson and Naukluft plateaus.
3. Analysis of the sedimentary architecture shows that the Greenheugh pediment capping unit contains three types of crossbedding, each representing deposition by morphologically distinct aeolian dunes. Compound cross-strata were deposited by oblique compound dunes; planar simple cross-bedding was deposited by straight-crested simple dunes; trough cross-bedding was deposited by either sinuous-crested simple dunes, or as part of a compound dune; and concordant compound cross-bedding, deposited by a dune formed by a fluctuating flow. The sedimentary architecture corresponds with other parts of the Stimson formation, indicating that sediment accumulation was controlled by aerodynamic processes.
4. Analysis of cross-set morphology and dip-azimuth allowed delineation of three distinct stratigraphic intervals, each recording a major change in sediment transport direction, further indicating a major change in sediment transport and wind direction. Within the Gleann Beag interval (deposited by oblique compound dunes), sediment was transported to the north or the northeast, reflecting sediment transport directions observed elsewhere in the Stimson formation. The Ladder interval (deposited by straight-crested simple dunes) records sediment transport to the south: uphill toward Mount Sharp, and the opposite direction to most sediment transport observed elsewhere in the Stimson. The Edinburgh interval (deposited by sinuous-crested simple dunes) records sediment transport to the west. The change in sediment transport at the Edinburgh interval corresponds to a change in geochemistry and mineralogy indicative of a different sedimentary provenance to that deposited in the Gleann Beag interval (Bedford et al., 2022; Thompson et al., 2022).
5. The different dune morphologies, and transport directions recorded provide evidence of a dynamic and changing climate, where the wind shifted over multiple temporal scales. First, intercalated avalanche and wind-ripple strata record high frequency shifts in wind direction: possibly seasonal changes. Second, longer-term seasonal trends are recorded by oblique compound dunes of the Gleann Beag interval and by flow reversal recorded at Ogre Hill by reactivation surfaces. Finally, long-term prolonged changes of wind direction are recorded by the opposed transport directions observed in the three different stratigraphic intervals, plus at Ogre Hill.
6. The Stimson formation is unlikely to represent a complete record of activity within the dune field. A major, prolonged reversal of sediment transport, recorded by the Ladder interval is coupled with a laterally extensive bounding surface, which may represent a deflationary supersurface. Reversing of the wind is a large-scale allogenic event and should be recorded across the Stimson dune field deposits. That it is only observed at the Greenheugh pediment indicates that the northern Stimson outcrops are incomplete records, where the top of the succession is missing.

Data Availability Statement

Data presented in this study are archived with the NASA Planetary Data System (pds.nasa.gov) and readily accessible through the MSL Curiosity Analyst's Notebook (https://an.rsl.wustl.edu/msl). Images used can be found in a data table in Text S1 in Supporting Information S1 slide pack. Data (interpretations) generated during the course of this study are available in Text S1 in Supporting Information S1.

Acknowledgments
The authors acknowledge the enormous efforts made by the NASA Mars Science Laboratory (MSL) Project's engineering, science, and management teams in making this work possible. The authors are also grateful to the many MSL team members who participated in tactical and strategic operations during the Glen Torridon campaign. Special thanks go to the Malin Space Science Systems operations team for their hard work in acquiring the extensive image data and software team for production of the Mastcam mosaic products used herein. Steven G. Banham, Sanjeev Gupta, and Robert Barnes acknowledge funding from the UK Space Agency (UKSA) (Grant numbers: ST/N000579/1; ST/S001492/1; ST/S001506/1; ST/T001755/1, ST/W002280/1). Gwénaël Caravaca was supported by the French space agency CNES under convention CNES 180027. VRVis are acknowledged for ongoing support and development of the PRo3D software. Joanneum Research are acknowledged for processing of key data products which made this research possible. VRVis and JOANNEUM RESEARCH activities were funded by ESA PRODEX contracts 4000105568 and 4000117520, as well as FFG ASAP Contract 882828. Data presented in this study are archived with the NASA Planetary Data System (pds.nasa.gov) and readily accessible through the MSL Curiosity Analyst's Notebook (https://an.rsl.wustl.edu/msl). Parts of this study were carried out at the Jet Propulsion Laboratory, California Institute of Technology, under a contract with the National Aeronautics and Space Administration. Reviewers Ryan Ewing and Charlie Bristow are acknowledged and thanked for their constructive comments during the review process: this manuscript has been improved by their input.

References

Abercrombie, S. P., Menzies, A., Winter, A., Clausen, M., Duran, B., Jorritsma, M., et al. (2017). OnSight: Multi-platform visualization of the surface of Mars. In *Paper presented at American geophysical union, fall meeting, december 01, 2017*. Retrieved from https://ui.adsabs.harvard.edu/abs/2017AGUFMED11C0134A

Ahlbrandt, T. S. (1979). Textural parameters of eolian deposits. In E. D. McKee (Ed.), *A study of global sand seas* (pp. 21–51). United States Geological Survey Professional Paper.

Alexander, D. A., Deen, R. G., Andres, P. M., Zamani, P., Mortensen, H. B., Chen, A. C., et al. (2006). Processing of Mars Exploration Rover imagery for science and operations planning. *Journal of Geophysical Research:Planets*, *111*(E2), E02S02. https://doi.org/10.1029/2005je002462

Almeida, R. P., Freitas, B. T., Turra, B. B., Figueiredo, F. T., Marconato, A., & Janikian, L. (2016). Reconstructing fluvial bar surfaces from compound cross-strata and the interpretation of bar accretion direction in large river deposits. *Sedimentology*, *63*(3), 609–628. https://doi.org/10.1111/sed.12230

Anderson, R., & Bell, J. (2010). Geologic mapping and characterization of Gale Crater and implications for its potential as a Mars Science Laboratory landing site. *MARS*, *5*, 76–128. https://doi.org/10.1555/mars.2010.0004

Anderson, R. B., Edgar, L. A., Rubin, D. M., Lewis, K. W., & Newman, C. (2018). Complex bedding geometry in the upper portion of Aeolis Mons, Gale crater, Mars. *Icarus*, *314*, 246–264. https://doi.org/10.1016/j.icarus.2018.06.009

Banham, S., Gupta, S., Bryk, A., Rubin, D., Edgett, K., Dietrich, W., et al. (2020). Does the Greenheugh pediment capping unit represent a continuation of the Stimson formation? In *Paper presented at LPSC 51*. Retrieved from https://www.hou.usra.edu/meetings/lpsc2020/pdf/2337.pdf

Banham, S. G., Gupta, S., Rubin, D. M., Edgett, K. S., Barnes, R., Van Beek, J., et al. (2021). A rock record of complex aeolian bedforms in a hesperian desert landscape: The Stimson formation as exposed in the Murray buttes, Gale crater, Mars. *Journal of Geophysical Research: Planets*, *126*(4). https://doi.org/10.1029/2020JE006554

Banham, S. G., Gupta, S., Rubin, D. M., Watkins, J. A., Sumner, D. Y., Edgett, K. S., et al. (2018). Ancient Martian aeolian processes and palaeomorphology reconstructed from the Stimson formation on the lower slope of Aeolis Mons, Gale crater, Mars. *Sedimentology*, *65*(4), 993–1042. https://doi.org/10.1111/sed.12469

Barnes, R., Gupta, S., Traxler, C., Ortner, T., Bauer, A., Hesina, G., et al. (2018). Geological analysis of Martian rover-derived digital outcrop models using the 3-D visualization tool, planetary robotics 3-D viewer—PRo3D. *Earth and Space Science*, *5*(7), 285–307. https://doi.org/10.1002/2018ea000374

Bedford, C. C., Banham, S. G., Bowden, D. L., Bridges, J. C., Forni, O., Cousin, A., et al. (2020). Identifying ancient dune processes in the Stimson formation of Gale crater from the Greenheugh pediment to the Emerson Plateau using geochemical data from ChemCam. In *AGU 2020 Fall meeting*.

Bedford, C. C., Banham, S. G., Bridges, J. C., Forni, O., Cousin, A., Bowden, D., et al. (2022). An insight into ancient Aeolian processes and post-noachian aqueous alteration in Gale crater, Mars, using ChemCam geochemical data from the Greenheugh capping unit. *Journal of Geophysical Research: Planets*, *127*, e2021JE007100. https://doi.org/10.1029/2021JE007100

Bedford, C. C., Schwenzer, S. P., Bridges, J. C., Banham, S., Wiens, R. C., Gasnault, O., et al. (2020). Geochemical variation in the Stimson formation of Gale crater: Provenance, mineral sorting, and a comparison with modern Martian dunes. *Icarus*, *341*, 113622. https://doi.org/10.1016/j.icarus.2020.113622

Bell, J. F., III, Godber, A., McNair, S., Caplinger, M. A., Maki, J. N., Lemmon, M. T., et al. (2017). The Mars Science Laboratory curiosity rover Mast camera (Mastcam) instruments: Pre-flight and in-flight calibration, validation, and data archiving. *Earth and Space Science*, *4*(7), 396–452. https://doi.org/10.1002/2016EA000219

Bennett, K. A., Fox, V. K., Bryk, A., Dietrich, W., Fedo, C., Edgar, L., et al. (2022a). The curiosity rover's exploration of Glen Torridon, Gale crater, Mars: An overview of the campaign and scientific results. *Journal of Geophysical Research: Planets*, *127*, e2022JE007185. https://doi.org/10.1029/2022JE007185

Bennett, K. A., Fox, V. K., Bryk, A. B., Dietrich, W. E., & Team, M. (2022b). An overview of key findings from the Curiosity rover's campaign in Glen Torridon, Gale crater, Mars. In *Paper presented at lunar and planetary conference* (Vol. 53).

Berner, R. A. (1968). Rate of concretion growth. *Geochimica et Cosmochimica Acta*, *32*(5), 477–483. https://doi.org/10.1016/0016-7037(68)90040-9

Blakey, R. C. (1988). Superscoops - their significance as elements of eolian architecture. *Geology*, *16*(6), 483–487. https://doi.org/10.1130/0091-7613(1988)016<0483:stsaeo>2.3.co;2

Boazman, S. J., Davis, J. M., Grindrod, P. M., Balme, M. R., Vermeesch, P., & Baird, T. (2021). Measuring ripple and dune migration in coprates chasma, valles marineris: A source to sink Aeolian system on Mars? *Journal of Geophysical Research: Planets*, *126*(3), e2020JE006608. https://doi.org/10.1029/2020JE006608

Brookfield, M. E. (1977). Origin of bounding surfaces in ancient aeolian sandstones. *Sedimentology*, *24*(3), 303–332. https://doi.org/10.1111/j.1365-3091.1977.tb00126.x

Brothers, S. C., Kocurek, G., Brothers, T. C., & Buynevich, I. V. (2017). Stratigraphic architecture resulting from dune interactions: White sands dune field, New Mexico. *Sedimentology*, *64*(3), 686–713. https://doi.org/10.1111/sed.12320

Calef, F. J., & Parker, T. (2016). MSL Gale merged Orthophoto mosaic, MSL team, PDS annex. *U.S. Geological Survey*. http://bit.ly/MSL_Basemap

Caravaca, G., Mangold, N., Dehouck, E., Schieber, J., Zaugg, L., Bryk, A. B., et al. (2022). From Lake to River: Documenting an Environmental Transition across the Jura/Knockfarril Hill Members Boundary in the Glen Torridon Region of Gale crater (Mars). *Journal of Geophysical Research: Planets*, *127*, e2021JE007093. https://doi.org/10.1029/2021JE007093

Cardenas, B. T., Kocurek, G., Mohrig, D., Swanson, T., Hughes, C. M., & Brothers, S. C. (2019). Preservation of Autogenic Processes and Allogenic Forcings in Set-Scale Aeolian Architecture II: The Scour-and-Fill Dominated Jurassic Page Sandstone, Arizona, U.S.A. *Journal of Sedimentary Research*, *89*(8), 741–760. https://doi.org/10.2110/jsr.2019.41

Chan, M. A., Archer, A. W., Sprinkel, D., Chidsey, T., & Anderson, P. (2000). Cyclic eolian stratification on the Jurassic Navajo Sandstone, Zion National Park: Periodicities and implications for paleoclimate. *Geology of Utah's Parks and Monuments*, *28*, 607–617.

Chojnacki, M., Banks, M. E., Fenton, L. K., & Urso, A. C. (2019). Boundary condition controls on the high-sand-flux regions of Mars. *Geology*, *47*(5), 427–430. https://doi.org/10.1130/g45793.1

Courrech du Pont, S. (2015). Dune morphodynamics. *Comptes Rendus Physique*, *16*(1), 118–138. https://doi.org/10.1016/j.crhy.2015.02.002

Courrech du Pont, S., Narteau, C., & Gao, X. (2014). Two modes for dune orientation. *Geology*, *42*(9), 743–746. https://doi.org/10.1130/G35657.1

Davis, J. M., Grindrod, P. M., Boazman, S. J., Vermeesch, P., & Baird, T. (2020). Quantified Aeolian Dune Changes on Mars Derived From Repeat Context Camera Images. *Earth and Space Science*, *7*(2), e2019EA000874. https://doi.org/10.1029/2019EA000874

De Hon, R. A., Barlow, N. G., Reagan, M. K., Bettis, E. A., III, Foster, C. T., Jr., Gulick, V. C., et al. (2001). Observation of the geology and geomorphology of the 1999 Marsokhod test site. *Journal of Geophysical Research*, *106*(E4), 7665–7682. https://doi.org/10.1029/1999je001167

Derickson, D., Kocurek, G., Ewing, R. C., & Bristow, C. (2008). Origin of a complex and spatially diverse dune-field pattern, Algodones, southeastern California. *Geomorphology*, *99*(1), 186–204. https://doi.org/10.1016/j.geomorph.2007.10.016

Dromart, G., Le Deit, L., Rapin, W., Anderson, R., Gasnault, O., Le Mouellic, S., et al. (2018). The Light-Toned Yardang Unit, Mount Sharp, Gale Crater, Mars Spotted by the Long Distance Remote Micro-Imager of ChemCam (MSL Mission). In *Paper presented at lunar and planetary science conference*.

Eastwood, E. N., Kocurek, G., Mohrig, D., & Swanson, T. (2012). Methodology for reconstructing wind direction, wind speed and duration of wind events from Aeolian cross-strata. *Journal of Geophysical Research:Earth Surface*, *117*(F3), F002368. https://doi.org/10.1029/2012jf002368

Edgar, L. A., Fedo, C. M., Gupta, S., Banham, S. G., Fraeman, A. A., Grotzinger, J. P., et al. (2020). A Lacustrine Paleoenvironment Recorded at Vera RubinRidge, Gale Crater: Overview of the Sedimentology and Stratigraphy Observed by the Mars ScienceLaboratory Curiosity Rover. *Journal of Geophysical Research: Planets*, *125*(3), e2019JE006307. https://doi.org/10.1029/2019je006307

Edgar, L. A., Gupta, S., Rubin, D. M., Lewis, K. W., Kocurek, G. A., Anderson, R. B., et al. (2017). Shaler: In situ analysis of a fluvial sedimentary deposit on Mars. *Sedimentology*, *65*(1), 96–122. https://doi.org/10.1111/sed.12370

Edgett, K. S., Yingst, R. A., Ravine, M. A., Caplinger, M. A., Maki, J. N., Ghaemi, F. T., et al. (2012). Curiosity's Mars Hand Lens Imager (MAHLI) Investigation. *Space Science Reviews*, *170*(1–4), 259–317. https://doi.org/10.1007/s11214-012-9910-4

Ehlmann, B. L., Edgett, K. S., Sutter, B., Achilles, C. N., Litvak, M. L., Lapotre, M. G. A., et al. (2017). Chemistry, Mineralogy, and Grain Properties at Namib and High Dunes, Bagnold Dune Field, Gale Crater, Mars: A Synthesis of Curiosity Rover Observations. *Journal of Geophysical Research: Planets*, *122*(12), 2510–2543. https://doi.org/10.1002/2017JE005267

Ewing, R. C., Kocurek, G., & Lake, L. W. (2006). Pattern analysis of dune-field parameters. *Earth Surface Processes and Landforms*, *31*(9), 1176–1191. https://doi.org/10.1002/esp.1312

Ewing, R. C., & Kocurek, G. A. (2010). Aeolian dune interactions and dune-field pattern formation: White Sands Dune Field, New Mexico. *Sedimentology*, *57*(5), 1199–1219. https://doi.org/10.1111/j.1365-3091.2009.01143.x

Ewing, R. C., Lapotre, M. G. A., Lewis, K. W., Day, M., Stein, N., Rubin, D. M., et al. (2017). Sedimentary processes of the Bagnold Dunes: Implications for the eolian rock record of Mars. *Journal of Geophysical Research: Planets*, *122*(12), 2544–2573. https://doi.org/10.1002/2017JE005324

Fedo, C., Grotzinger, J., Bryk, A., Bennett, K., Fox, V., Stein, N., et al. (2020). Ground-based stratigraphic correlation of the Jura and Knockfarril Hill members of the Murray formation, Gale crater: Bridging the Vera Rubin ridge-Glen Torridon divide. In *Paper presented at 51st lunar and planetary science conference*.

Fedo, C., Grotzinger, J., Gupta, S., Stein, N., Watkins, J., Banham, S., et al. (2017). Facies analysis and basin architecture of the upper part of the Murray formation, Gale Crater, Mars. In *Paper presented at lunar and planetary science conference XLVIII*. Retrieved from https://www.hou.usra.edu/meetings/lpsc2017/pdf/1689.pdf

Fedo, C. M., Bryk, A. B., Edgar, L. A., Bennett, K. A., Fox, V. K., Dietrich, W. E., et al. (2022). Geology and stratigraphic correlation of the Murray and Carolyn Shoemaker formations across the Glen Torridon region, Gale crater, Mars. *Journal of Geophysical Research: Planets*, *127*, e2022JE007408. https://doi.org/10.1029/2022JE007408

Folk, R. L. (1980). *Petrology of sedimentary rocks*. Hemphill Publishing Company. (p. 185).

Fraeman, A. A., Edgar, L. A., Rampe, E. B., Thompson, L. M., Frydenvang, J., Fedo, C. M., et al. (2020). Evidence for a Diagenetic Origin of Vera Rubin Ridge, Gale Crater, Mars: Summary and Synthesis of Curiosity's Exploration Campaign. *Journal of Geophysical Research: Planets*, *125*(12), e2020JE006527. https://doi.org/10.1029/2020JE006527

Fraeman, A. A., Ehlmann, B. L., Arvidson, R. E., Edwards, C. S., Grotzinger, J. P., Milliken, R. E., et al. (2016). The stratigraphy and evolution of lower Mount Sharp from spectral, morphological, and thermophysical orbital data sets. *Journal of Geophysical Research:Planets*, *121*(9), 1713–1736. https://doi.org/10.1002/2016je005095

Fryberger, S. G., & Schenk, C. J. (1988). Pin stripe lamination - A distinctive feature of modern and ancient eolian sediments. *Sedimentary Geology*, *55*(1–2), 1–15. https://doi.org/10.1016/0037-0738(88)90087-5

Fryberger, S. G., Schenk, C. J., & Krystinik, L. F. (1988). Stokes surfaces and the effects of near-surface groundwater-table on aeolian deposition. *Sedimentology*, *35*(1), 21–41. https://doi.org/10.1111/j.1365-3091.1988.tb00903.x

Garzanti, E. (2017). The Maturity Myth In Sedimentology and Provenance Analysis. *Journal of Sedimentary Research*, *87*(4), 353–365. https://doi.org/10.2110/jsr.2017.17

Garzanti, E., Resentini, A., Ando, S., Vezzoli, G., Pereira, A., & Vermeesch, P. (2015). Physical controls on sand composition and relative durability of detrital minerals during ultra-long distance littoral and aeolian transport (Namibia and southern Angola). *Sedimentology*, *62*(4), 971–996. https://doi.org/10.1111/sed.12169

Gillespie, M., Stephenson, D., & Millward, D. (2008). *BGS classification of lithodemic units: Proposals for classifying units of intrusive rock Report*. British Geological Survey. Retrieved from http://nora.nerc.ac.uk/id/eprint/5226/

Grant, J. A., Wilson, S. A., Mangold, N., Calef, F., III, & Grotzinger, J. P. (2014). The timing of alluvial activity in Gale crater, Mars. *Geophysical Research Letters*, *41*(4), 1142–1148. https://doi.org/10.1002/2013gl058909

Greeley, R., & Iversen, R. D. (1985). *Wind as a geological process* (p. 333). Cambridge University Press.

Grotzinger, J. P., Crisp, J. A., & Vasavada, A. R., & M. S. L. S. Team. (2015). Curiosity's Mission of Exploration at Gale Crater, Mars. *Elements*, *11*(1), 19–26. https://doi.org/10.2113/gselements.11.1.19

Grotzinger, J. P., Gupta, S., Malin, M. C., Rubin, D. M., Schieber, J., Siebach, K., et al. (2015). Deposition, exhumation, and paleoclimate of an ancient lake deposit, Gale crater, Mars. *Science*, *350*(6257), 177–191. https://doi.org/10.1126/science.aac7575

Grotzinger, J. P., Sumner, D. Y., Kah, L. C., Stack, K., Gupta, S., Edgar, L., et al. (2014). A Habitable Fluvio-Lacustrine Environment at Yellowknife Bay, Gale Crater, Mars. *Science*, *343*(6169), 1242777. https://doi.org/10.1126/science.1242777

Gwizd, S., Fedo, C., Grotzinger, J., Banham, S., Rivera-Hernández, F., Stack, K. M., et al. (2022). Sedimentological and geochemical perspectives on a marginal lake environment recorded in the Hartmann's Valley and Karasburg members of the Murray formation, Gale crater, Mars. *Journal of Geophysical Research: Planets*, *127*(8), e2022JE007280. https://doi.org/10.1029/2022je007280

Gwizd, S., Fedo, C., Grotzinger, J., Edgett, K., Rivera-Hernández, F., Gupta, S., et al. (2020). Transition from a Lacustrine Margin to a Lacustrine Basin in Gale Crater, Mars: The Hartmann's Valley and Karasburg Members of the Murray Formation. In *Paper presented at LPSC 51*. Retrieved from https://www.hou.usra.edu/meetings/lpsc2020/pdf/2719.pdf

Gwizd, S., Fedo, C., Grotzinger, J., Edgett, K., Rivera-Hernandez, F., & Stein, N. (2018). Depositional History of the Hartmann's Valley Member, Murray Formation, Gale Crater, Mars. In *Paper presented at lunar and planetary science conference*.

Hanson, W. R. (1991). *Suggestions to authors of the reports of the United States geological Survey* (p. 311). Report. Retrieved from http://pubs.er.usgs.gov/publication/7000088

Havholm, K. G., & Kocurek, G. (1988). A preliminary study of the dynamics of a modern draa, Algodones, southeastern California, USA. *Sedimentology*, *35*(4), 649–669. https://doi.org/10.1111/j.1365-3091.1988.tb01242.x

Havholm, K. G., & Kocurek, G. (1994). Factors controlling aeolian sequence stratigraphy - Clues from super bounding surface-features in the middle Jurassic Page Sandstone. *Sedimentology*, *41*(5), 913–934. https://doi.org/10.1111/j.1365-3091.1994.tb01432.x

Hayes, A. G., Grotzinger, J. P., Edgar, L. A., Squyres, S. W., Watters, W. A., & Sohl-Dickstein, J. (2011). Reconstruction of eolian bed forms and paleocurrents from cross-bedded strata at Victoria Crater, Meridiani Planum, Mars. *Journal of Geophysical Research:Planets*, *116*(E7), E003688. https://doi.org/10.1029/2010je003688

Hunter, R. E. (1977). Basic types of stratification in small eolian dunes. *Sedimentology*, *24*(3), 361–387. https://doi.org/10.1111/j.1365-3091.1977.tb00128.x

Hunter, R. E. (1985). Subaqueous sand-flow cross strata. *Journal of Sedimentary Research*, *55*(6), 886–894. https://doi.org/10.1306/212f8832-2b24-11d7-8648000102c1865d

Hunter, R. E., & Richmond, B. M. (1988). Daily cycles in coastal dunes. *Sedimentary Geology*, *55*(1), 43–67. https://doi.org/10.1016/0037-0738(88)90089-9

Hunter, R. E., & Rubin, D. M. (1983). Interpreting cyclic cross-bedding, with an example from the Navajo Sandstone. In M. E. Brookfield & T. S. Ahlbrandt (Eds.), *Eolian sediments and processes* (pp. 429–454). Elsevier. https://doi.org/10.1016/S0070-4571(08)70808-2

Jerolmack, D. J., Mohrig, D., Grotzinger, J. P., Fike, D. A., & Watters, W. A. (2006). Spatial grain size sorting in eolian ripples and estimation of wind conditions on planetary surfaces: Application to Meridiani Planum, Mars. *Journal of Geophysical Research:Planets*, *111*(E5), E002544. https://doi.org/10.1029/2005je002544

Kocurek, G. (1981). Significance of interdune deposits and bounding surfaces in aeolian dune sands. *Sedimentology*, *28*(6), 753–780. https://doi.org/10.1111/j.1365-3091.1981.tb01941.x

Kocurek, G. (1991). Interpretation of ancient eolian sand dunes. *Annual Review of Earth and Planetary Sciences*, *19*(1), 43–75. https://doi.org/10.1146/annurev.earth.19.1.43

Kocurek, G., Carr, M., Ewing, R., Havholm, K. G., Nagar, Y. C., & Singhvi, A. K. (2007). White Sands Dune Field, New Mexico: Age, dune dynamics and recent accumulations. *Sedimentary Geology*, *197*(3), 313–331. https://doi.org/10.1016/j.sedgeo.2006.10.006

Kocurek, G., & Day, M. (2017). What is preserved in the aeolian rock record? A Jurassic Entrada Sandstone case study at the Utah–Arizona border. *Sedimentology*, *65*(4), 1301–1321. https://doi.org/10.1111/sed.12422

Kocurek, G., & Dott, R. H. (1981). Distinctions and uses of stratification types in the interpretation of eolian sand. *Journal of Sedimentary Petrology*, *51*(2), 579–595. https://doi.org/10.1306/212F7CE3-2B24-11D7-8648000102C1865D

Kuenen, P. H. (1960). Experimental Abrasion 4: Eolian Action. *The Journal of Geology*, *68*(4), 427–449. https://doi.org/10.1086/626675

Lancaster, N. (1995). *Geomorphology of desert dunes*. Psychology Press.

Le Deit, L., Hauber, E., Fueten, F., Pondrelli, M., Rossi, A. P., & Jaumann, R. (2013). Sequence of infilling events in Gale Crater, Mars: Results from morphology, stratigraphy, and mineralogy. *Journal of Geophysical Research:Planets*, *118*(12), 2439–2473. https://doi.org/10.1002/2012je004322

Lindholm, R. (1987). *A practical approach to sedimentology* (p. 276). Allen & Unwin. https://doi.org/10.1007/978-94-011-7683-5

Lindquist, S. J. (1988). Practical characterization of eolian reservoirs for development: Nugget Sandstone, Utah—Wyoming thrust belt. *Sedimentary Geology*, *56*(1), 315–339. https://doi.org/10.1016/0037-0738(88)90059-0

Maki, J., Thiessen, D., Pourangi, A., Kobzeff, P., Litwin, T., Scherr, L., et al. (2012). The Mars Science Laboratory Engineering Cameras. *Space Science Reviews*, *170*(1–4), 77–93. https://doi.org/10.1007/s11214-012-9882-4

McDonald, R. R., & Anderson, R. S. (1995). Experimental verification of aeolian saltation and lee side deposition models. *Sedimentology*, *42*(1), 39–56. https://doi.org/10.1111/j.1365-3091.1995.tb01270.x

McEwen, A. S., Eliason, E. M., Bergstrom, J. W., Bridges, N. T., Hansen, C. J., Delamere, W. A., et al. (2007). Mars Reconnaissance Orbiter's High Resolution Imaging Science Experiment (HiRISE). *Journal of Geophysical Research: Planets*, *112*(E5), E002605. https://doi.org/10.1029/2005je002605

McKee, E. D., & Weir, G. W. (1953). Terminology for Stratification and Cross-Stratification in Sedimentary Rocks. *GSA Bulletin*, *64*(4), 381–390. https://doi.org/10.1130/0016-7606(1953)64[381:TFSACI]2.0.CO;2

Milliken, R. E., Ewing, R. C., Fischer, W. W., & Hurowitz, J. (2014). Wind-blown sandstones cemented by sulfate and clay minerals in Gale Crater, Mars. *Geophysical Research Letters*, *41*(4), 1149–1154. https://doi.org/10.1002/2013gl059097

Moore, H. J. (1971). Geologic interpretation of lunar data. *Earth-Science Reviews*, *7*(1), 5–33. https://doi.org/10.1016/0012-8252(71)90002-X

Mountney, N. P. (2006). Periodic accumulation and destruction of aeolian erg sequences in the Permian Cedar Mesa Sandstone, White Canyon, southern Utah, USA. *Sedimentology*, *53*(4), 789–823. https://doi.org/10.1111/j.1365-3091.2006.00793.x

Mountney, N. P., & Russell, A. J. (2009). Aeolian dune-field development in a water table-controlled system: Skeiðarársandur, Southern Iceland. *Sedimentology*, *56*(7), 2107–2131. https://doi.org/10.1111/j.1365-3091.2009.01072.x

Mountney, N. P., & Thompson, D. B. (2002). Stratigraphic evolution and preservation of aeolian dune and damp/wet interdune strata: An example from the Triassic Helsby Sandstone Formation, Cheshire Basin, UK. *Sedimentology*, *49*(4), 805–833. https://doi.org/10.1046/j.1365-3091.2002.00472.x

NACSN (2005). North American stratigraphic codeRep. *1558–9153*, pp.1547–1591.

Nesbit, P. R., Boulding, A. D., Hugenholtz, C. H., Durkin, P. R., & Hubbard, S. M. (2020). Visualization and Sharing of 3D Digital Outcrop Models to Promote Open Science. *Geological Society of America Today*, *30*(6), 4–10. https://doi.org/10.1130/GSATG425A.1

Nield, J. M., Wiggs, G. F. S., Baddock, M. C., & Hipondoka, M. H. T. (2017). Coupling leeside grainfall to avalanche characteristics in aeolian dune dynamics. *Geology*, *45*(3), 271–274. https://doi.org/10.1130/g38800.1

Paar, G., & Consortium, P. (2016). PRoViDE Final Report. http://www.provide-space.eu/wp-content/uploads/2015/01/PRVD-REP-JR-Final-Report_2016-04-14-Public.pdf

Paar, G., Waugh, L., Barnes, D., Pajdla, T., Woods, M., Graf, H.-R., et al. (2012). Integrated field testing of planetary robotics vision processing: The PRoVisG campaign in Tenerife 2011. In *Paper presented at intelligent robots and computer vision XXIX: Algorithms and techniques*. International Society for Optics and Photonics. https://doi.org/10.1117/12.906410

Pedersen, A., Kocurek, G., Mohrig, D., & Smith, V. (2015). Dune deformation in a multi-directional wind regime: White Sands Dune Field, New Mexico. *Earth Surface Processes and Landforms*, *40*(7), 925–941. https://doi.org/10.1002/esp.3700

Phillips, J., Ewing, R., Bowling, R., Weymer, B. A., Barrineau, P., Nittrouer, J., & Everett, M. (2019). Low-angle eolian deposits formed by protodune migration, and insights into slipface development at White Sands Dune Field, New Mexico. *Aeolian Research*, *36*, 9–26. https://doi.org/10.1016/j.aeolia.2018.10.004

Rapin, W., Dromart, G., Rubin, D., Le Deit, L., Mangold, N., Edgar, L. A., et al. (2021). Alternating wet and dry depositional environments recorded in the stratigraphy of Mount Sharp at Gale crater, Mars. *Geology*. https://doi.org/10.1130/g48519.1

Rubin, D. M. (1987). Cross-bedding, bedforms, and Paleocurrents. *SEPM Concepts in sedimentology and paleontology*, *1*, 187. https://doi.org/10.2110/csp.87.01

Rubin, D. M. (2012). A unifying model for planform straightness of ripples and dunes in air and water. *Earth-Science Reviews*, *113*(3), 176–185. https://doi.org/10.1016/j.earscirev.2012.03.010

Rubin, D. M., & Carter, C. L. (2006). *Cross-bedding, bedforms, and paleocurrents* (p. 195). SEPM. https://doi.org/10.2110/csp.87.01

Rubin, D. M., & Hunter, R. E. (1983). Reconstructing Bedform Assemblages from Compound Crossbedding. In M. E. Brookfield & T. S. Ahlbrandt (Eds.), *Developments in sedimentology* (pp. 407–427). Elsevier. https://doi.org/10.1016/S0070-4571(08)70807-0. Retrieved from http://www.sciencedirect.com/science/article/pii/S0070457108708070

Rubin, D. M., & Hunter, R. E. (1985). Why deposits of longitudinal dunes are rarely recognized in the geologic record. *Sedimentology*, *32*(1), 147–157. https://doi.org/10.1111/j.1365-3091.1985.tb00498.x

Rubin, D. M., & Hunter, R. E. (1987). Bedform alignment in directionally varying flows. *Science*, *237*(4812), 276–278. https://doi.org/10.1126/science.237.4812.276

Scherer, C. M. S., & Goldberg, K. (2010). Cyclic cross-bedding in the eolian dunes of the Sergi Formation (Upper Jurassic), Recoincavo Basin: Inferences about the wind regime. *Palaeogeography, Palaeoclimatology, Palaeoecology*, *296*(1–2), 103–110. https://doi.org/10.1016/j.palaeo.2010.06.018

Schieber, J., Bish, D., Coleman, M., Reed, M., Hausrath, E. M., Cosgrove, J., et al. (2017). Encounters with an unearthly mudstone: Understanding the first mudstone found on Mars. *Sedimentology*, *64*(2), 311–358. https://doi.org/10.1111/sed.12318

Sharp, R. P. (1963). Wind ripples. *The Journal of Geology*, *71*(5), 617–636. https://doi.org/10.1086/626936

Smith, D. E., Zuber, M. T., Frey, H. V., Garvin, J. B., Head, J. W., Muhleman, D. O., et al. (2001). Mars Orbiter Laser Altimeter: Experiment summary after the first year of global mapping of Mars. *Journal of Geophysical Research*, *106*(E10), 23689–23722. https://doi.org/10.1029/2000je001364

Stack, K. M., Grotzinger, J. P., Lamb, M. P., Gupta, S., Rubin, D. M., Kah, L. C., et al. (2019). Evidence for plunging river plume deposits in the Pahrump Hills member of the Murray formation, Gale crater, Mars. *Sedimentology*, *66*(5), 1768–1802. https://doi.org/10.1111/sed.12558

Stein, N. T., Quinn, D. P., Grotzinger, J. P., Fedo, C., Ehlmann, B. L., Stack, K. M., et al. (2020). Regional Structural Orientation of the Mount Sharp Group Revealed by In Situ Dip Measurements and Stratigraphic Correlations on the Vera Rubin Ridge. *Journal of Geophysical Research: Planets*, *125*(5), e2019JE006298. https://doi.org/10.1029/2019JE006298

Sullivan, R., & Kok, J. (2017). Aeolian saltation on Mars at low wind speeds. *Journal of Geophysical Research: Planets*, *122*(10), 2111–2143. https://doi.org/10.1002/2017JE005275

Sullivan, R., Kok, J. F., Katra, I., & Yizhaq, H. (2020). A Broad Continuum of Aeolian Impact Ripple Morphologies on Mars is Enabled by Low Wind Dynamic Pressures. *Journal of Geophysical Research: Planets*, *125*(10), e2020JE006485. https://doi.org/10.1029/2020JE006485

Tanaka, K. L., Skinner, J. A., Dohm, J. M., Irwin, R. P., III, Kolb, E. J., Fortezzo, C. M., et al. (2014). Geologic map of MarsRep. 2329-132X. *US Geological Survey*. https://doi.org/10.3133/sim3292

Thompson, L., Spray, J., O'Connell-Cooper, C., Berger, J., Yen, A., Boyd, N., et al. (2022). Alteration at the base of the siccar point unconformity and further evidence for an alkaline provenance at Gale crater: Exploration of the mount sharp group, Greenheugh pediment cap rock contact with APXS. *Earth and Space Science Open Archive*. https://doi.org/10.1002/essoar.10510037.1

Thomson, B. J., Bridges, N. T., Milliken, R., Baldridge, A., Hook, S. J., Crowley, J. K., et al. (2011). Constraints on the origin and evolution of the layered mound in Gale Crater, Mars using Mars Reconnaissance Orbiter data. *Icarus*, *214*(2), 413–432. https://doi.org/10.1016/j.icarus.2011.05.002

Traxler, C., Ortner, T., Hesina, G., Barnes, R., Gupta, S., Paar, G., et al. (2018). The PRoViDE Framework: Accurate 3D geological models for virtual exploration of the Martian surface from rover and orbital imagery. In A. Bistacchi, L. Jorda, M. Massironi, & S. Viseur (Eds.), *3D digital geological models: From terrestrial outcrops to planetary surfaces*. John Wiley & Sons.

Uličný, D. (2004). A drying-upward aeolian system of the Bohdašín Formation (Early Triassic), Sudetes of NE Czech Republic: Record of seasonality and long-term palaeoclimate change. *Sedimentary Geology*, *167*(1), 17–39. https://doi.org/10.1016/j.sedgeo.2004.01.014

Vasavada, A. R., Grotzinger, J. P., Arvidson, R. E., Calef, F. J., Crisp, J. A., Gupta, S., et al. (2014). Overview of the Mars Science Laboratory mission: Bradbury Landing to Yellowknife Bay and beyond. *Journal of Geophysical Research:Planets*, *119*(6), 1134–1161. https://doi.org/10.1002/2014je004622

Vicente-Retortillo, Á., Martínez, G. M., Renno, N., Newman, C. E., Ordonez-Etxeberria, I., Lemmon, M. T., et al. (2018). Seasonal Deposition and Lifting of Dust on Mars as Observed by the Curiosity Rover. *Scientific Reports*, *8*(1), 17576. https://doi.org/10.1038/s41598-018-35946-8

Viúdez-Moreiras, D., Gómez-Elvira, J., Newman, C. E., Navarro, S., Marin, M., Torres, J., & de la Torre-Juárez, M. (2019). Gale surface wind characterization based on the Mars Science Laboratory REMS dataset. Part II: Wind probability distributions. *Icarus*, *319*, 645–656. https://doi.org/10.1016/j.icarus.2018.10.010

Warner, N., Silverman, M., Samuels, J., DeFlores, L., Sengstacken, A., Maki, J., et al. (2016). The Mars Science Laboratory Remote Sensing Mast. In *Paper presented at 2016 IEEE aerospace conference, big sky*. https://doi.org/10.1109/AERO.2016.7500554

Watkins, J. A., Grotzinger, J., Stein, N., Banham, S. G., Gupta, S., Rubin, D., et al. (2016). Paleotopography of Erosional Unconformity, Base of Stimson Formation, Gale Crater, Mars. In *Paper presented at lunar and planetary science conference*. Retrieved from http://adsabs.harvard.edu/abs/2016LPI.47.2939W

Watkins, J. A., Grotzinger, J. P., Stein, N. T., Banham, S. G., Gupta, S., Rubin, D. M., et al. (2022). Burial and exhumation of sedimentary rocks revealed by the base Stimson erosional unconformity, Gale crater, Mars. *Journal of Geophysical Research: Planets*, *127*(7), e2022JE007293. https://doi.org/10.1029/2022je007293

Weitz, C. M., Sullivan, R. J., Lapotre, M. G. A., Rowland, S. K., Grant, J. A., Baker, M., & Yingst, R. A. (2018). Sand Grain Sizes and Shapes in Eolian Bedforms at Gale Crater, Mars. *Geophysical Research Letters*, *45*(18), 9471–9479. https://doi.org/10.1029/2018GL078972

Wilkinson, M., & Dampier, M. D. (1990). The rate of growth of sandstone-hosted calcite concretions. *Geochimica et Cosmochimica Acta*, *54*(12), 3391–3399. https://doi.org/10.1016/0016-7037(90)90293-T

Wilson, I. G. (1972). Aeolian bedforms - Their development and origins. *Sedimentology*, *19*(3–4), 173–210. https://doi.org/10.1111/j.1365-3091.1972.tb00020.x

Yingst, R. A., Edgett, K. S., Kennedy, M. R., Krezoski, G. M., McBride, M. J., Minitti, M. E., et al. (2016). MAHLI on Mars: Lessons learned operating a geoscience camera on a landed payload robotic arm. *Geoscientific Instrumentation Methods and Data Systems*, *5*(1), 205–217. https://doi.org/10.5194/gi-5-205-2016